Polymer-Based 3-D Printed 140-220 GHz Low-Cost Quasi-Optical Components and Integrated Subsystem Assembly

SANG-HEE SHIN [1], (Graduate Student Member, IEEE),
XIAOBANG SHANG [2], (Senior Member, IEEE), **NICK M. RIDLER** [2], (Fellow, IEEE),
AND STEPAN LUCYSZYN [1], (Fellow, IEEE)

[1] Department of Electrical and Electronic Engineering, Imperial College London, London SW7 2AZ, U.K.
[2] National Physical Laboratory, Department of Electromagnetic and Electrochemical Technologies, Teddington TW11 0LW, U.K.

Corresponding author: Stepan Lucyszyn (s.lucyszyn@imperial.ac.uk)

ABSTRACT Few examples of individual polymer-based 3-D printed quasi-optical component types have been previously demonstrated above *ca.* 100 GHz. This paper presents the characterization of polymer-based 3-D printed components and complete subsystems for quasi-optical applications operating at G-band (140 to 220 GHz). Two low-cost consumer-level 3-D printing technologies (vat polymerization and fused deposition modeling) are employed, normally associated with microwave frequencies and longer wavelength applications. Here, five different quasi-optical component types are investigated; rectangular horn antennas, 90° off-axis parabolic mirrors, radiation absorbent material (RAM), grid polarizers and dielectric lenses. As an alternative to conventional electroplating, gold-leaf gilding is used for the polarizer. A detailed investigation is undertaken to compare the performance of our 3-D printed antennas, mirrors and RAM with their commercial equivalents. In addition, a fully 3-D printed, RAM-lined housing with central two-axis rotational platform is constructed for performing two-port measurements of a quasi-optical horn-mirror-polarizer-mirror-horn subsystem. Measured results generally show excellent performances, although the grid polarizer is limited by the minimum strip width, separation distance and metallization thickness. The ultra-low cost, 'plug and play' housing is designed to give a fast measurement setup, while minimizing misaligning losses. Its RAM lining is designed to suppress reflections due to diffraction from components under test that may cause adverse multi-path interference. Our work investigates each component type at G-band and integrates them within subsystem assemblies; operating at frequencies well above those normally associated with low-cost consumer-level 3-D printing technologies. This opens-up new opportunities for rapid prototyping of complete low-cost front-end quasi-optical upper-millimeter-wave subsystems.

INDEX TERMS Additive manufacturing, 3-D printing, millimeter-wave, G-band, WR-5, quasi-optical, horn antenna, parabolic mirror, RAM, grid polarizer, dielectric lens.

I. INTRODUCTION

Additive manufacturing using polymer-based 3-D printing is an emerging technology that is finding its way from academic research to commercial exploitation; not least for mobile and aerospace applications (such as unmanned balloons and drones, manned aircraft and space stations, satellites and

The associate editor coordinating the review of this manuscript and approving it for publication was Diego Masotti.

interplanetary spacecraft), where mass is an important driver. This enabling technology has already proven itself with metal-pipe rectangular waveguides (MPRWGs) and associated components. For example, the authors have already demonstrated waveguides using various polymer-based 3-D printing technologies: fused deposition modelling (FDM) at X-band (8 to 12 GHz) [1]; polymer-jetting (PolyJet) at Ku-band (12 to 18 GHz) [2], [3]; stereolithographic apparatus (SLA) at W-band (75 to 110 GHz) [1]; PolyJet in the WM-570

S.-H. Shin *et al.*: Polymer-Based 3-D Printed 140-220 GHz Low-Cost Quasi-Optical Components and Integrated Subsystem Assembly

IEEE *Access*

band (325 to 500 GHz) [4]; and RECILS in the WM-380 band (500 to 750 GHz) and WM-250 band (750 GHz to 1.1 THz) [5].

Quasi-optics relates to components that are comparable in size to the wavelength of the associated electromagnetic radiation. Like guided-wave structures, quasi-optical components can be difficult, slow and expensive to manufacture. They often require computer-aided high-precision machining and polishing equipment. However, current advancement in additive manufacturing technologies are showing great potential for manufacturing quasi-optical components in fast and cost-effective ways. To this end, at G-Band (140 to 220 GHz), the authors previously undertook an elementary imaging study of a rectangular horn antenna feeding an 90° off-axis parabolic mirror; both components were 3-D printed using PolyJet technology [6].

The following represents a review of 3-D printed (sub-)millimeter-wave quasi-optical components, of the types investigated later in this paper. It should be noted that for each, less than a handful of polymer-based 3-D printed examples could be found in the open literature for upper-millimeter-wave (*ca.* 100 to 300 GHz) and sub-millimeter-wave/terahertz (0.3 to 3 THz) frequency applications.

A. HORN ANTENNAS

Horn antennas are commonly used in quasi-optical systems, as an interface between a waveguide medium and free space. As with conventional MPRWGs, horn antennas operating between 0.1 and 3 THz are very expensive. As a result, there is growing interest in low-cost manufacturing of horn antennas using 3-D printing technologies.

Metal-based 3-D printed antennas have demonstrated good performance. However, these relatively expensive manufacturing technologies still require post-processing to overcome inherent surface-roughness problems [7], [8].

With polymer-based 3-D printing, in 2011, Timbie *et al.* reported a split-block corrugated horn antenna operating over most of W-band using SLA technology [9]. Later, in 2016, Decrossas *et al.* demonstrated a W-band split-block corrugated horn antenna using a PolyJet 3-D printer [10]. In 2012, Macor *et al.* from SWISSto12 demonstrated a conical smooth wall horn antenna operating at 92.5 GHz using SLA technology [11]. Later, in 2014, Bieren *et al.* from the same team, reported a diagonal horn antenna operating in the WR-3.4 band (220 to 330 GHz) using SLA technology [12]. More recently, in 2018, Molaei *et al.*, demonstrated a PolyJet 3-D printed rectangular horn antenna operating at E-band (60 to 90 GHz) [13]. With all these examples, no direct performance comparison is made with an equivalent commercial counterpart. However, a comparison was made with an E-band SLA 3-D printed antenna (coated with silver spray paint) and compared with a commercial counterpart (electroformed with copper) and it was found that the gain was improved by an average of approximately 1 dB [14]. In summary, all these 3-D printing technologies have proven themselves suitable for manufacturing mm-wave and THz horn antennas using industrial-level 3-D printers.

In contrast, an ultra-low cost masked stereolithographic apparatus (MSLA) 3-D printer is employed here to fabricate ruggedized rectangular horn antennas, which are then deployed in fully 3-D printed subsystem demonstrators. Moreover, the performance of our modified replica antennas have been investigated and benchmarked against their commercial counterpart.

B. PARABOLIC MIRRORS

Typically, a parabolic mirror is used to either tightly focus a collimated beam or to collimate a diverging beam, where beam divergence emanates from an effective focal point. With quasi-optical systems, 90° off-axis parabolic mirrors (OAPMs) are commonplace. These mirrors have very specific 3-D surface curvatures (cut across a circular paraboloid, in our case), requiring a minimum accuracy dictated by a small fraction of the smallest wavelength of operation λ_{min} (e.g., $\lambda_{min}/20$). Therefore, for optical applications, accurate computer numerical control (CNC) machining and polishing processes are required. However, for (sub-)mm-wave applications, 3-D printing offers new opportunities, as demonstrated by the authors at 160 GHz using PolyJet technology [6]. At the same time, in Jul. 2018, Romeu *et al.* explored three different types of 3-D printing technologies (SLA, FDM and Multi Jet Fusion) for fabricating larger mirrors for operation at 100 GHz [15]. The measured beam profiles are comparable to their commercial counterpart. In 2019, Fullager *et al.* demonstrated a mirror similar to that previous demonstrated [6], but manufactured with a low-cost desktop SLA 3-D printer and tested at 530 GHz [16]. The measured beam profiles, determined using a THz camera (with sufficiently high source power and relatively high camera resolution), are comparable to their commercial counterpart.

In this work, we use the new Formlabs Low Force Stereolithography (LFS)^{TM} 3-D printer technology [17], based on a type of SLA technology, to manufacture mass-reduced mirrors, which are then deployed in fully 3-D printed subsystem demonstrators and benchmarked against their commercial counterparts.

C. RADIATION ABSORBENT MATERIAL

Radiation absorbent material (RAM) is used in anechoic chambers to reduce unwanted reflections, as it mitigates against adverse multi-path interference and standing-waves in line-of-sight paths. RAM can be manufactured with numerous combinations of polymers having magnetic and/or electric nanoparticle fillers. For example, Huber *et al.* [18] characterized 3-D printable polylactic acid (PLA) polymer composite materials in the microwave frequency range of 2 to 10 GHz: conductive PLA and magnetic PLA.

With lossy composite thermoplastic filaments, for FDM 3-D printers, there has been some attempts to fabricate free-space absorbers at microwave frequencies. For example, truncated pyramidal and frequency selective surface (FSS) metamaterial absorbers have been developed by Kjelgard *et al.*, operating from 2.6 to 4 GHz and 6 to 8.5 GHz, respectively [19]. Both absorbers are 3-D printed

IEEE *Access*

S.-H. Shin *et al.*: Polymer-Based 3-D Printed 140-220 GHz Low-Cost Quasi-Optical Components and Integrated Subsystem Assembly

using Proto-pasta conductive PLA [20], made by ProtoPlant Inc. (USA).

In 2016, Arbaoui *et al.*, characterized a carbon-loaded Acrylonitrile Butadiene Styrene (ABS) polymer (TW-CON175BK, from Torwell Technologies) for use as a broadband microwave waveguide matched load termination across X-band [21].

In 2019, Petroff *et al.* developed a 3-D wedge-shaped RAM (broadband graded index absorber designed around a geometric approximation of the space-filling Hilbert curve) using carbon-loaded high impact polystyrene (HIPS) composite filament. The return loss (without metallic backing) is better than 22 dB, at normal incidence, in two different frequency bands: 63 to 115 GHz and 140 to 215 GHz [22].

In our work, Proto-pasta conductive PLA tessellating pyramidal-array RAM is FDM 3-D printed as zig-saw tiles and characterized from 140 to 220 GHz and benchmarked against their commercial equivalent. The bespoke RAM tiles line the inside of a quasi-optical housing, which are then deployed in fully 3-D printed subsystem demonstrators.

D. GRID POLARIZER

In quasi-optical systems, a grid polarizer is a spatial filter that lets incident radiation of a specific polarization to pass through, while (partially-)blocking radiation with other polarizations.

Proto-pasta conductive PLA has also been used to develop an absorbing grid polarizer, for frequencies between 500 GHz and 2.7 THz. With strip widths and separation of 300 μm, extinction ratios better than 20 dB are demonstrated, with performance depending on the strip thicknesses (varying between 1 and 5 mm) [23]. However, this cannot be used as a reflection-transmission beam splitter due to its highly absorbing nature.

Ryu *et al.* developed a grid polarizer with a type of SLA printer that uses the Texas Instruments digital micro-mirror projection system, with ultraviolet (UV)-curable acrylate-based resin [24]. This polarizer has a strip width and separation of 132 μm and 268 μm, respectively. The strips are sputter-coated with 100 nm thick gold, which lines the front face and 792 μm thick sidewalls. The maximum extinction ratio is only 2.3 dB over their measured grid-effect frequency range from 2.94 to 2.50 THz [24]. The reason for this poor performance is that they operate above the theoretical transverse-electric (TE) cut-off frequency of 0.56 THz.

In this work, we demonstrate a low-cost grid polarizer using FDM 3-D printing and gold-leaf gilding, operating from 140 to 187 GHz. This is tested in our fully 3-D printed housing.

E. DIELECTRIC LENSES

As with the OAPM (in reflection mode), dielectric lenses (in transmission mode) are used to collimate and focus beams in (quasi-)optical systems. However, fabricating a custom lens using conventional CNC machining can be very expensive, especially if aspherical profiles and/or larger diameters are

needed. Utilizing the inherent design flexibility offered by 3-D printing, a number of lens antennas and quasi-optical lenses have been demonstrated at millimeter(mm)-wave frequencies.

Using a PolyJet 3-D printer, Yi *et al.* reported dielectric lens antennas, having geometrically complex anti-reflection structures, operating from 50 to 70 GHz and 220 to 325 GHz [25]. Chudpooti *et al.* demonstrated hemispherical lens antennas operating from 220 to 320 GHz, manufactured using low-cost digital light processing (DLP) 3-D printer technology [26]. Although these examples prove that these 3-D printing technologies are suitable for fabricating mm-wave dielectric lens antennas, they were not tested for quasi-optical beam collimation/focusing applications.

Using a Multi-Jet-Modelling 3-D printing technology, three types of lenses (symmetric, elliptical-aspheric, planar-hyperbolic) were demonstrated for quasi-optical applications at 200 GHz; results show very accurate focal lengths [27]. More recently, in 2019, Friel *et al.* demonstrated a PLA-based FDM 3-D printed hyperbolic lens, with wavelength specific anti-reflective surface structures optimized for 60 GHz, having reasonably accurate focal points [28].

Our work concentrates on using the ultra-low cost MSLA 3-D printer to fabricate two hyperbolic aspherical plano-convex lenses (conventional lens and thin Fresnel lens).

F. QUASI-OPTICAL HOUSING

In general, commercial machined breadboards and compatible mounts are used for (quasi-)optical prototyping; all having very high mechanical accuracy and requiring manual alignment, which is a very slow and expensive solution for the measurement of individual components and their integrated subsystems.

Unlike with optical experiments, beam alignment in quasi-optical systems can be very difficult to achieve, without laborious micrometer adjustments to the many individual positioners (each having multiple degrees of freedom). This is because visible laser alignment techniques are not always possible. Moreover, with multiple components interacting with the beam path, replacing any one component may require other components to be re-aligned.

One solution is to create a special housing, with pre-aligned slots that can facilitate the 'plug and play' concept for individual components, without requiring re-alignment. While consumer-level 3-D printing may not currently have the mechanical accuracy for shorter wavelength optical experiments, it will be shown here that longer wavelength quasi-optical systems are possible.

To our knowledge, after an exhaustive search, only two examples of a 3-D printed quasi-optical housing have been reported in the open literature, both published by the same group at Harris Corp. (USA) at 39 GHz in 2018 [29] and 60 GHz and 100 GHz in 2019 [30]. Their rigid plastic frame is 3-D printed, to create an air cavity for supporting two open-ended rectangular waveguides having a line-of-sight distance of fifteen wavelengths ($15\lambda_o$) in free space.

S.-H. Shin *et al.*: Polymer-Based 3-D Printed 140-220 GHz Low-Cost Quasi-Optical Components and Integrated Subsystem Assembly

IEEE *Access*

TABLE 1. Calculations and reported measurements [29], [30] of quasi-optical lens systems for coupling between open-ended waveguides.

Frequency (GHz)	Our Assumed Waveguide Band			Our Calculations		Reported Measured Results	
	EIA Designation	Internal Aperture Dimensions (mm)		Open-ended Waveguide Directivity (dBi)	Friis Transmission Path Loss Without Lenses (dB)	Insertion Loss Without Lenses (dB)	Focusing Gain (dB)
		a	b				
39 [29]	WR-22	5.6896	2.8448	5.37	35.1	32.5	18.6
60 [30]	WR-15	3.7592	1.8796	5.51	34.5	–	18.3
100 [30]	WR-10	2.5400	1.2700	6.54	32.4	–	22.1

In addition, two biconvex lenses and their supports are 3-D printed; the 100 GHz implementation also has 3-D printed rail alignment structures, designed for use with multiple inter-lock points on the frame. The material of choice for the lens, supports and alignment structures is Cyanate Ester 220 (CE 220), printed using a continuous liquid interface production (CLIP^{TM}) technology on the very expensive Carbon M1 3-D printer. This material is selected because of its flat frequency response dielectric properties between 20 to 57 GHz, measured using an open-resonator test system; the extracted band-average dielectric constant is 2.49 and loss tangent is 0.013 [29], [31]. Harris Corp. then state that CE 221 is used, as it is easier to print and post-process, while keeping the same electrical properties as CE 220. In their proof-of-concept demonstrators, they record the improvement in insertion loss, between the open-ended waveguides when lenses are introduced, which they term 'focusing gain'. The reported values of measured insertion loss (without lenses) and focusing gain are given in Table 1, along with our textbook calculations for Friis transmission path loss (without lenses): $-20log_{10}\{(a \times b)/\lambda_o R\}$, where $R \simeq 15\lambda_o$ is the path length between the open-ended waveguides, both having internal width a and height b dimensions based on an assumption of the standard Electronic Industry Alliance (EIA) waveguide bands used. This ideal scenario also assumes 100% efficient radiation from both MPRWG apertures and so our calculated path losses are underestimated. It can be seen in Table 1 that the measured insertion loss (without lenses) is within 3 dB of our prediction at 39 GHz. At this frequency, the quasi-optical lens system demonstrates a 14 dB port-to-port insertion loss for the coupling between two MPRWGs.

In addition to the five individual quasi-optical component types, a bespoke quasi-optical housing is developed to provide a rapid low transmission path loss measurement environment with a low-cost 'plug and play' integrated subsystem assembly. This contrasts greatly with the much smaller and simpler quasi-optical lens system, demonstrated by Harris Corp., for their objective of *"efficiently coupling RF energy from one waveguide to another across a pre-determined distance"* [30].

II. DESIGN
A. HORN ANTENNAS
A commercial Flann Microwave Ltd 20 dBi standard gain rectangular horn antenna (model #30240-20) is chosen [32]

for replication. This is commercially manufactured by copper electroforming on precision mandrels, to ensure high accuracy and repeatability. These standard gain antennas are very well understood and there is a comprehensive datasheet available enabling replica 3-D printed versions to be made [32].

For G-band, the rectangular waveguide has WR-5 standard internal aperture dimensions of only 1,295 μm × 647.5 μm (this is equivalent to the WM-1295 waveguide size in the IEEE standard [33]). The linearly tapered horn antenna has a flare length of 14.5 mm, with maximum internal aperture dimensions of 6.8 mm × 5.0 mm, and overall length of 17.5 mm. From these dimensions, assuming infinitesimally thin metal walls and a perfect electrical conductor (PEC), the theoretical directivity is $4\pi A/\lambda_o^2$ for any aperture antenna; giving 20.85 dBi at 160 GHz, where the maximum internal aperture area $A = 34$ mm^2 and free-space wavelength $\lambda_0(160 \text{ GHz}) = 1.8737$ mm. As previously observed [2], in practice, the reduction in gain due to finite wall conductivity can be effectively compensated for by the reduction in lost power in the backlobes (since backward radiation leakage caused by knife-edge diffraction is reduced with finite wall thickness).

At 160 GHz, the calculated far-field (or Fraunhofer/Rayleigh) distance $z_{ff} = 2D_A^2/\lambda_0(160\text{GHz}) = 76.0$ mm, with the largest internal aperture dimension $D_A = 8.44$ mm.

To increase structural rigidity and reduce structural stress concentrations at sharp corners, regions with relatively thin walls are thickened and sharp corners rounded. In addition, buttresses have been added between the horn and flange, to reduce warpage caused by the post-UV curing process. The flange design is based on IEEE standard specifications [34]. Figure 1 shows the fabricated ruggedized 3-D printed modified replica horn antenna.
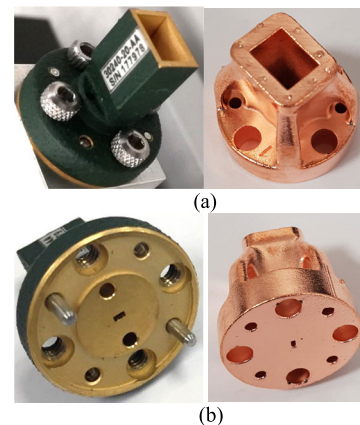

FIGURE 1. Photographs of commercial counterpart (left) and ruggedized 3-D printed modified replica (right) G-band rectangular horn antennas: (a) showing horn aperture; (b) showing flange aperture.

B. 90° OFF-AXIS PARABOLIC MIRROR
A commercial Edmund Optics Ltd 90° OAPM (original model #63-188, with #35-522 replacement) is chosen for benchmarking against, with specifications given

in Table 2 [35] and the associated ray tracing illustrated in Fig. 2.

TABLE 2. Commercial 90° off-axis parabolic mirror specifications [35].

Parameters	Values
Mirror Diameter, D	76.2 mm
Off-Axis Angle	90º
Parent Focal Length, f_{pa}	38.1 mm
Y Offset, y_{off}	76.2 mm
Reflected Effective Focal Length, f_{eff}	76.2 mm
Substrate and Coating Material	Protected Aluminum
Intended Optical Wavelength Range	400 to 700 nm
RMS Surface Roughness	17.5 nm
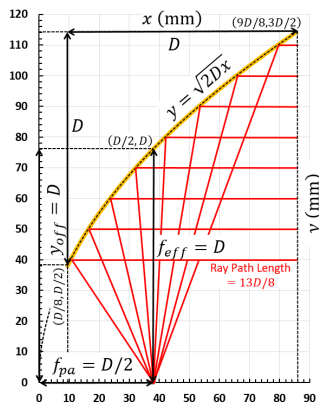
FIGURE 2. Ray tracing for the 90° off-axis parabolic mirror.

The parabolic surface of the mirror represents a complex 3-D curved structure that tests the limits of 3-D printing technology, in terms of achievable resolution and print orientation that both affect accuracy and surface roughness; these need to be at least $\lambda_{min}(220 \text{ GHz})/20 = 68 \mu\text{m}$ at the worst-case G-band frequency of 220 GHz.

Rectangular waveguides support higher-order modes at frequencies above their recommended operating band. In contrast, optical mirrors can potentially operate at mm-wave frequencies (with the lower limit dictated by diffraction), throughout the terahertz (THz) frequency band (0.3 to 3 THz) and beyond (with the upper frequency limit dictated by metal conductivity and surface roughness losses).

To reduce weight, unnecessary material underneath the mirror surface is removed. As with the horn antenna, support pillars are added to reduce warpage and add structural rigidity. Moreover, to reduce structural stress concentrations, sharp corners are rounded. The commercial counterpart and 3-D printed modified replica 90° OAPMs are shown in Fig. 3.

C. RADIATION ABSORBENT MATERIAL

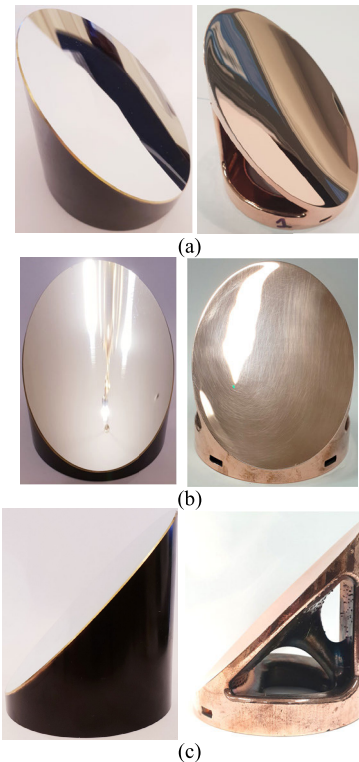Ultra-wideband RAM can be realized using naturally absorbing materials and wave impedance transforming geometries.

FIGURE 3. Photographs of commercial counterpart (left) and mass-reduced 3-D printed modified replica (right) 90° off-axis parabolic mirrors: (a) isometric views; (b) front views; and (c) side views.

One common example is carbon-loaded polymer, shaped into a 2-D array of pyramids. Here, tessellating pyramidal-array RAM is FDM 3-D printed using Proto-pasta conductive PLA. This polymer composite is made with Natureworks 4043D PLA, a dispersant and 20% conductive carbon black powder [20].

Due to the nature of FDM 3-D printing, the tips of the pyramids cannot be infinitesimally small. In practice, the top of the pyramid has dimensions of 0.5 mm $\times$ 0.5 mm. The base of the pyramid has dimensions of 5 mm $\times$ 5 mm, which is large enough to be structurally stable during 3-D printing. The height of our pyramid is 7 mm, which is long enough to provide a gentle taper into the absorbing medium, enabling operation down to microwave frequencies. Finally, a 1 mm thick base is added to provide increased absorption (and reduced transmission) and structural stability. Figure 4 shows the key dimensions and a fabricated 18 $\times$ 26 pyramidal-array tile for the FDM 3-D printed RAM.

D. GRID POLARIZER

Ideally, the strip width, thickness and separation distance need to be as small as possible. With our linear polarizer, the 400 μm strip width is defined by the FDM 3-D printer's nominal minimum extrusion line width of 400 μm. To avoid strips touching, while allowing variations in extrusion line widths and gold-leaf gilding, the chosen strip separation distance is $h = 800$ μm. As a result, the theoretical TE upper cut-off
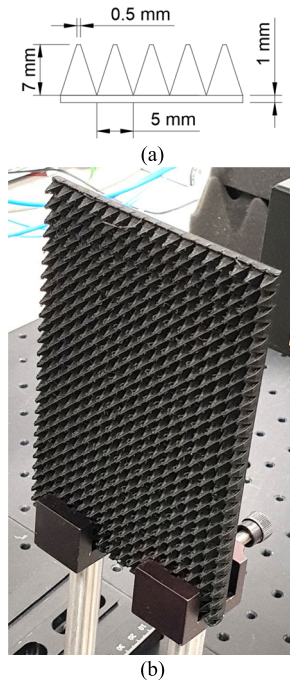
S.-H. Shin *et al.*: Polymer-Based 3-D Printed 140-220 GHz Low-Cost Quasi-Optical Components and Integrated Subsystem Assembly

IEEE *Access*

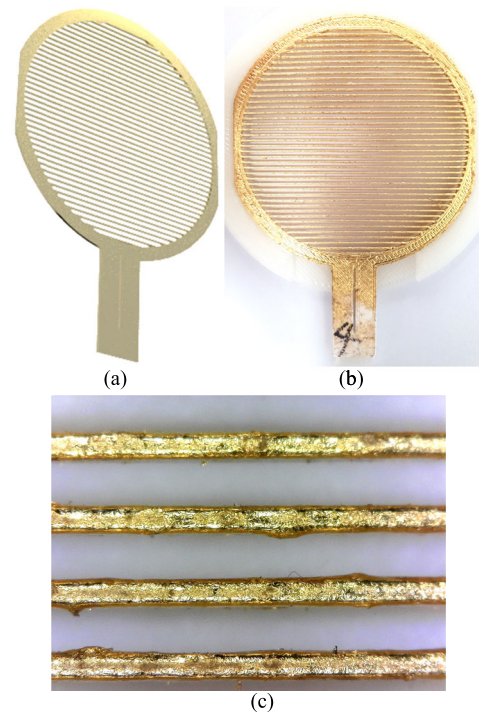**FIGURE 4.** FDM 3-D printed pyramidal RAM: (a) cross-sectional CAD drawing; and (b) photograph.

FIGURE 5. 3-D printed and gold-leaf gilded grid polarizer: (a) CAD rendering; (b) photograph; and (c) zoomed-in view photograph.

frequency is $f_c = c/2h = 187.37$ GHz, where c is the speed of light in free space.

For structural rigidity, eight extrusion lines are printed on top of one another, giving a total thickness of 800 μm. On top of this, three layers of 24 carat (fineness of 99.99) gold leaf is gilded, giving a total metallization thickness of approximately 0.36 μm. At the worst-case G-band frequency of 140 GHz, the skin depth $\delta = 1/\sqrt{\pi f \mu_o \sigma_o} = 0.21$ μm, where μ_o is the permeability of free space and the bulk conductivity of gold at DC is $\sigma_o = 4.1 \times 10^7$ S/m. Therefore, with a total metallization thickness of only $T_m = 1.714\delta$ (instead of the recommended minimum thickness of 5δ), limited grid polarizer performance is to be expected from our ultra-low cost implementation. For example, as a flat continuous gold sheet, the absorption (or penetration) loss of electromagnetic energy as it propagates through the three sheets is $-10log_{10}\left\{ e^{-2T_m/\delta} \right\} = 15$ dB; while its shielding effectiveness would be much higher. Figure 5 shows the design and final realization of the grid polarizer.

E. QUASI-OPTICAL HOUSING

Our fully 3-D printed quasi-optical housing is designed for two-port measurements, with a horn-mirror-mirror-horn (HMMH) path and a two-axis rotational platform at the center to support the devices under test (DUT). With reference to Fig. 6, the entire housing frame is FDM 3-D printed as a single piece, having maximum outer dimensions of 270 mm $\times$ 219 mm $\times$ 102 mm. Two rectangular slots are provided for the horn antennas, and their mechanical interface adapters,
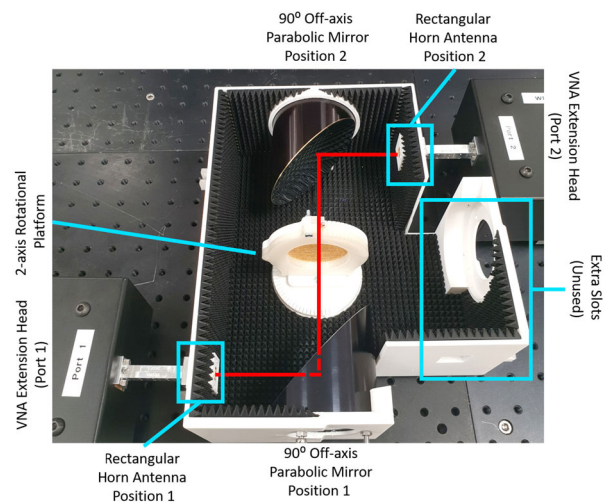

FIGURE 6. 3-D printed quasi-optical housing with commercial horns and mirrors assembled here for polarizer measurements (signal path indicated in red).

associated with Ports 1 and 2 of the vector network analyzer (VNA) and its frequency extension heads.

Circular slots are also provided for up to three 90° off-axis parabolic mirrors. In Fig. 6, two mirrors are shown, which collimate the diverging incident beams from the horn antennas, with the DUT's rotating platform positioned midway between mirrors. This platform is intended for measuring the polarizer, as shown in Fig. 6, and RAM. As mentioned previously, the inner walls of the housing are lined with our FDM 3-D printed RAM.

The spatial design of the housing was the result of a number of practical constraints and required the use of geometrical ray tracing and full-wave electromagnetic (EM) simulations.

For example, the orientation of the HMMH arrangement is important. It is recommended that the two OAPMs have coinciding axes for the parent parabolas [36]; this optimal arrangement results in minimal aberrations due to source misalignments. As a result, the frequency extension heads need to be located side-by-side, such that both reference ports are facing the same direction. However, a VNA and its frequency extension heads are calibrated such that both reference ports are in-line and facing each other in opposite directions.

To reduce instrumentation errors, associated with the coaxial cables (local oscillator, RF and reference signals) connecting the VNA to the frequency extension heads, Virginia Diodes (VDI) recommends that cable bending and movement should be minimized to avoid introducing significant phase mismatching; with sensitivity increasing as wavelength decreases. For this reason, the orientation of our HMMH arrangement is such that the two OAPMs are rotated 180° about their common optical axis [36]; being more susceptible to aberrations due to source misalignments. Therefore, housing slots for the rectangular horn antennas are orientated to face in opposite directions, as shown in Fig. 6.

Another consideration is the spatial distance between mirrors, since the distance between the horn and associated mirror is fixed by the focal length. Since there is a DUT placed between mirrors, which may be rotated, there has to be sufficient separation distance. Conversly, the maximum distance of 207.6 mm, between center points, is dictated by the maximum build volume capacity of our FDM 3-D printer.

To verify the focal positions of the HMMH arrangement, 2-D ray tracing is undertaken with MATLAB coding, and the results are shown in Fig. 7(a). Clearly, with our arrangement, assuming an ideal point-source and perfect alignment, the beam diverges, collimates and converges perfectly with identical focal distances of 76.2 mm at each port.

In practice, with quasi-optics, the minimum insertion loss is obtained when the positioning of all the HMMH components are optimized. A horn antenna does not represent the ideal point source. For this reason, the effective equivalent point source and focal point locations within the flare of the horn antenna must be established. To do this, EM simulations using HFSS and ray tracing are combined. With the former, a 2-D slice of the radiating horn antenna boresight beam profile is recorded at a distance of 80 mm from the radiating aperture. Then the $1/e^2$ beamwidth boundaries are determined for both the E- and H-field planes. To speed up this process, only 1-D slices are recorded in the E- and H-field planes, at distances of 50, 60 and 70 mm. Finally, rays are traced back to the propagation z-axis. Note that the $1/e^2$ beamwidths against z-axis distance get closer to a linear relationship as z increases; with our values from 50 to 80 mm being large enough to undertake this extrapolation. As shown in Fig. 7(b), the results reveal optimal focal points at 0.97 mm and 3.5 mm inside the horn antenna for the E- and H-field
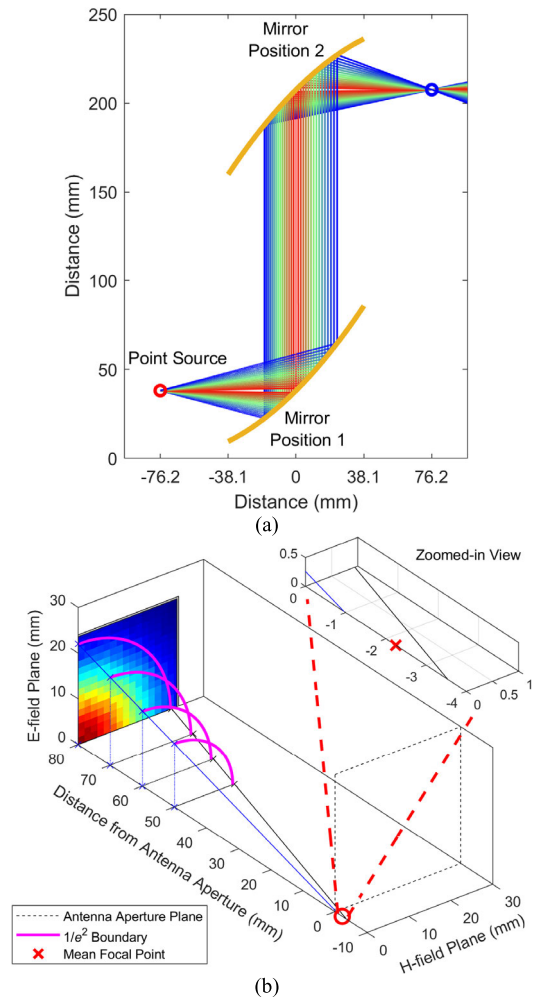

FIGURE 7. Ray tracing for determining quasi-optical component positions: (a) our HMMH arrangement having the two OAPMs rotated 180° about their common optical axis; and (b) effective equivalent focal point inside the rectangular horn antenna.

planes, respectively. For this reason, the slots for the horn antennas are positioned to be aligned near the arithmetic mean value of 2.25 mm, between these two focal points.

F. DIELECTRIC LENSES

To design dielectric lenses, the material first needs to be characterized. Elegoo Water Washable Rapid Resin (Ceramic Grey) is the material used here, as it is capable of producing parts to a relatively very high accuracy with ultra-low cost 3-D printing. To characterize the dielectric properties at G-band, 4 mm and 6 mm thick disk samples are MSLA 3-D printed and tested with the SWISSto12 WR-5 material characterization kit (MCK) at the UK's National Physical Laboratory (NPL) [37]. The extracted dielectric constant ε_r and loss tangent across G-band are shown in Fig. 8.

Using the G-band average dielectric constant value of $\varepsilon_r = 2.89$ (with refractive index $n \simeq \sqrt{\varepsilon_r} = 1.7$), a hyperbolic aspherical plano-convex lens is designed. In theory, this type of lens can provide a perfect focal point without spherical
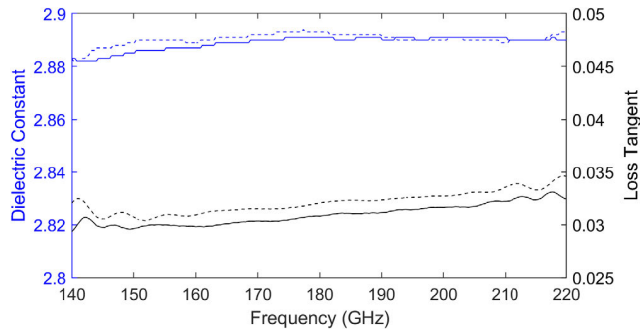
S.-H. Shin *et al.*: Polymer-Based 3-D Printed 140-220 GHz Low-Cost Quasi-Optical Components and Integrated Subsystem Assembly

IEEE *Access*

FIGURE 8. Extracted dielectric constant (blue lines) and loss tangent (black lines) for the 4 mm (dotted lines) and 6 mm (solid lines) samples.

aberration. The curvature profile of the lens can be derived using textbook expressions. For any given lens radius r, the free-space optical path length from the curvature of the lens to the focal point $OPL(r)$ is given by:

$$OPL(r) = \sqrt{\left(f_{pl} + z(r)\right)^2 + r^2} \qquad (1)$$

where, the target focal path length f_{pl} is the minimum distance from the lens to the focal point (along the optical axis) and $z_{max} - z(r)$ represents the lens curvature profile with z_{max} representing the maximum thickness of the lens (with $r = 0$). The optical path length at the center of the lens (OPL_c) is:

$$OPL_c = f_{pl} + \sqrt{\varepsilon_r} \cdot z(r) \qquad (2)$$

Hence, equating (1) and (2) gives:

$$z^2(r)\left(\varepsilon_r - 1\right) + 2f_{pl}z(r)\left(\sqrt{\varepsilon_r} - 1\right) - r^2 = 0 \qquad (3)$$

Using the quadratic expression in (3), $z(r)$ can be extracted as a function of radius, up to our chosen maximum target value of $r = r_{max}$. Using Snell's law, a MATLAB code is written for a target focal path length $f_{pl} = 76.2$ mm and lens diameter of $2r_{max} = 60$ mm, giving $z_{max} = 7.45$ mm, with optical ray tracing results shown in Fig. 9(a). This clearly shows that the profile provides a perfect focal point without any spherical aberration. In practice, to minimize warpage during the post-UV curing process, a 1 mm thick base and a 2 mm thick rim at the edge of the lens are added. The key spatial dimensions and a photograph of the 3-D printed hyperbolic aspherical plano-convex lens are shown in Fig. 9(b) and (c), respectively.

Using the same hyperbolic profile describe previously, a plano-convex Fresnel lens is designed. The thickness of the original lens is sliced into seven 2 mm thick layers, which are then collapsed to create the characteristic Fresnel lens cross-sectional profile. Since the basic Fresnel lens thickness does not exceed 2 mm, the upper limit on its diameter is not dictated by dielectric losses, as would be the case with the conventional lenses. For this reason, the Fresnel lens diameter is increased to 80 mm. In practice, a 1 mm thick base and a 2.4 mm thick rim at the edge of the lens are added to minimize warpage. The key spatial dimensions and a photograph of the 3-D printed Fresnel lens are shown in Fig. 10(a) and (b), respectively.
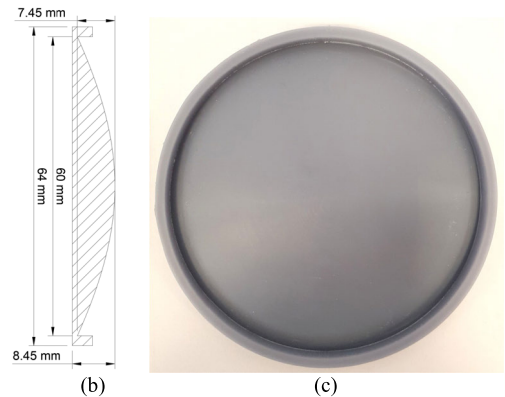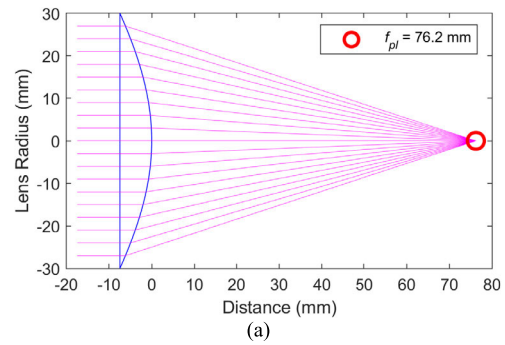

FIGURE 9. Hyperbolic aspherical plano-convex conventional lens: (a) optical ray tracing diagram; (b) cross-sectional CAD drawing; and (c) photograph.
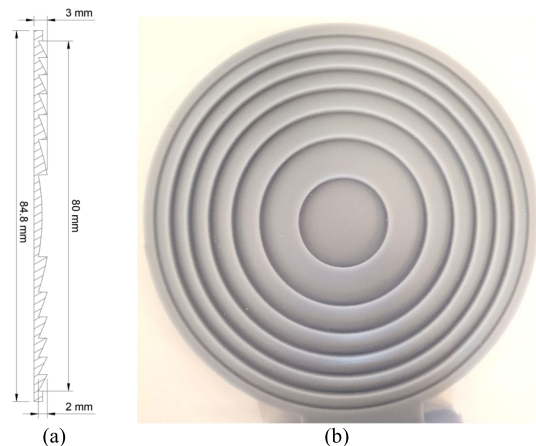

FIGURE 10. Hyperbolic aspherical plano-convex Fresnel lens: (a) cross-sectional CAD drawing; and (b) photograph.

III. FABRICATION

Two different generic types of 3-D printing technologies are used in this work: (i) vat photopolymerization with UV cured photopolymer resin, employing both MSLA and SLA; and (ii) fused deposition modeling with PLA-based thermoplastic filaments. All the 3-D printed CAD models are drawn using Autodesk Fusion 360, with maximum triangular mesh refinement setting to maintain the integrity of curved surfaces.

A. VAT PHOTOPOLYMERIZATION

To fabricate the rectangular horn antennas, a low-cost desktop MSLA printer, Elegoo Mars, is employed with upgraded

linear rails and bearings (costing approximately $350). This printer utilizes a 2K resolution UV liquid crystal display (LCD) screen, as a mask for illuminating and curing the resin. This provides prints with ultra-high resolution (quoted by the manufacturer as 47 μm × 47 μm × 20 μm [38]) and well-defined corner and edge features. However, due to its relatively small build volume (with maximum dimension of 120 mm × 68 mm × 155 mm [38]) and visible voxel boundaries (with certain print scenarios), it is not optimal for the 90° OAPM.

3-D CAD models for the rectangular horn antenna and the lenses are set to a 20 μm layer-height using the Chitubox slicer software [39]. The slicer also adds support material to some outer surfaces of the rectangular horn antenna. Internal and flange surfaces are avoided, to ensure maximum dimensional accuracy and to minimize the need for mechanical post processing. Elegoo Water Washable Rapid Resin (Ceramic Grey) is used, as it provides high precision and low shrinkage.

After the 3-D printing has completed, the parts are post processed at room temperature (to minimize warpage) with the following steps: (i) pre-rinse in a water bath at room-temperature; (ii) mechanical support structure removal; (iii) water-jet cleaning; (iv) 30 minutes in an ultrasonic bath, to remove any residual uncured resin; (v) drying with compressed air; and (vi) post UV-cure. After a short exposure (below 10 minutes) under the weak UV lamp, to solidify the outer surface, the parts are left under natural light for a number of hours; this slowly continues the curing process.

To fabricate the 90° OAPM, the Formlab's Form 3 printer is used (costing approximately $3,500). This SLA printer employs a 250 mW UV laser for illuminating (at normal incidence) and curing the resin. The Form 3 is capable of producing parts with high resolution (quoted by the manufacturer as 20 μm × 20 μm × 20 μm [17]) and relatively large build volume (145 mm × 145 mm × 185 mm [17]). These attributes make it suitable for fabricating the 90° OAPM. Formlab's Grey resin is used, as it is suitable for applications that require smooth surface finish and high accuracy. 3-D CAD models for the 90° OAPM are sliced to a layer-height of 20 μm using the PreForm slicer software [40]. In this case, support material is only added to non-reflecting surfaces, to avoid compromising the integrity of the mirror's curvature.

Parts produced from Form 3 require slightly different post processing, when compared to Elegoo Mars. The finished parts are post processed at room temperature using the following steps: (i) pre-rinse in isopropanol (IPA); (ii) mechanical support structure removal; (iii) surface cleaning using a fine brush; (iv) 15 minutes agitating in an IPA bath; (v) drying with compressed air; and (vi) post UV-cure. After a short exposure (below 10 minutes) under the weak UV lamp, to solidify the outer surface, the parts are left under natural light for a number of hours.

B. FUSED DEPOSITION MODELING
To fabricate the RAM, grid polarizer and quasi-optical housing (with additional two-axis rotating platform), the Raise3D

Pro 2 is employed (costing approximately $4,000). This FDM 3-D printer has a maximum build volume of 280 mm × 305 mm × 300 mm [41], which makes it ideal for manufacturing large single piece components. With its 400 μm diameter nozzle, it can reliably achieve our preferred layer height of 200 μm. 3-D CAD models for these components are sliced for printing using the IdeaMaker slicer software [42].

For the grid polarizer and quasi-optical housing, Raise 3D generic white PLA is used, while Proto-pasta conductive PLA is used for the RAM. In principle, while both the RAM and the quasi-optical housing can be co-printed (using dual extrusion), to reduce material waste, the RAM is printed separately into zig-saw bespoke tile pieces and snapped into place.

C. METALIZATION
The 3-D printed rectangular horn antennas and 90° OAPM are commercially coated. First a thin electroless-plated nickel seed layer is deposited, followed by a 50 μm thick electroplated layer of copper (corresponding to 287 skin depths at the worst-case G-band frequency of 140 GHz). Finally, polishing (OAPM only) and an anti-tarnishing post-processing treatment is applied.

The grid polarizer is too thin for conventional plating. Initially, we investigated the application of 842AR Super Shield^{TM} silver conductive liquid coating (one-part durable acrylic lacquer, pigmented with an extremely conductive silver flake), having a quoted resistivity of 110 $\mu\Omega \cdot$ cm [43]. However, due to its high viscosity, the coating was uneven. An alternative could be to use the Jet Metal^{TM} silver spray metallization process, which is reported to have a thickness dependent volume resistivity that matches pure bulk silver of 1.59 $\mu\Omega \cdot$ cm, with 2.5 to 3 μm thick layers [14]. Instead, we chose to try gold-leaf gilding, with bulk gold having a volume resistivity at DC of approximately 2 $\mu\Omega \cdot$ cm; this material is preferred, as both silver and copper tarnish over time.

The gold leaf thickness is approximately 0.12 μm and so multiple layers are needed. The 3-D printed grid polarizer is pre-heated on a 60 °C hotplate and coated with 3 layers of gold leaf (corresponding to 1.7 skin depths at 140 GHz), using low-viscosity acrylic gilding glue.

D. ANTENNA AND MIRROR WEIGHT COMPARISON
Mass is of great importance for some applications and so it is interesting to compare the various commercial counterparts with their 3-D printed modified replicas. To this end, all the components are weighed, and the results are given in Table 3. It can be clearly seen that additive manufacturing using polymer-based 3-D printing and metal plating offers a considerable weight saving; with our modified replicas being less than a third the mass of their commercial counterparts.

IV. G-BAND ANTENNA AND LENS MEASUREMENTS
All electromagnetic measurements were undertaken within the Department of Electromagnetic and Electrochemical

S.-H. Shin et al.: Polymer-Based 3-D Printed 140-220 GHz Low-Cost Quasi-Optical Components and Integrated Subsystem Assembly

IEEE Access

TABLE 3. Weight comparison for commercial counterpart reference and 3-D printed and plated modified replicas.

Component	Average Mass (g)		
	Commercial Counterpart	Modified Replica	Mass Ratio
Horn Antenna	12.5 (copper)	3.5	3.6
Parabolic Mirror	499 (aluminum)	130	3.8

Technologies at the U.K.'s National Physical Laboratory, using their Keysight Technologies PNA-X N5247B vector network analyzer – with VDI WR-5.1 frequency extender heads [44] – and the 1024 pixel TeraSense TERA-1024 (sub-)THz imaging camera [45] from Imperial College London.

A. HORN ANTENNAS

A semi-open anechoic environment is constructed, primarily using commercial 100 mm × 100 mm tessellating pyramidal-array RAM tiles, positioned in strategic locations (e.g., antenna boresight and above the quasi-optical breadboard). These tiles are made from solid carbon-loaded polypropylene plastic [46], manufactured by Thomas-Keating Ltd., demonstrating good measured performance from 20 to 180 GHz [47] and recommended for operation from below 50 GHz to above 1 THz [48]. In addition, 6 mm thick flexible foam sheet broadband microwave absorber was cut to surround other strategic locations (e.g., surrounding the back of the horn antennas and covering the metal frequency extension head boxes), as shown in Fig. 11(a). This RAM is Eccosorb®AN-72, made from multilayer carbon-loaded polyurethane foam, designed to reflect less than 17 dB of normal incident energy above 20 GHz, relative to a metal plate [49].

With the commercial counterpart and ruggedized 3-D printed modified replica antennas facing the RAM, their input return loss are measured, as shown in Fig. 11(a), with the results shown in Fig. 11(b). Across the whole of G-band, the commercial reference antenna has a return loss better than 25 dB. With our ruggedized 3-D printed antennas, the worst-case return loss is 12 dB across the whole of G-band, and approximately 20 dB from 150 to 200 GHz; demonstrating good performance with this first test scenario. The discrepancy in performance can be attributed to the lower manufacturing tolerance of the flange that has been fabricated with our low-cost MSLA 3-D printer. The low frequency Fabry-Pérot ripples (with frequency period $\Delta f \sim 20$ GHz) corresponding to the antenna flare length ($c/\Delta f \sim 14.5$ mm).

To evaluate the transmission performance, each antenna is connected in turn to Port 1, while facing a reference commercial antenna connected to Port 2; the line-of-sight aperture-to-aperture separation distance $R = 185$ mm. During the measurements, the facing horn-horn antenna pair is surrounded with commercial RAM, as shown in Fig. 12(a). A commercial horn-horn antenna pair is also tested as a reference.
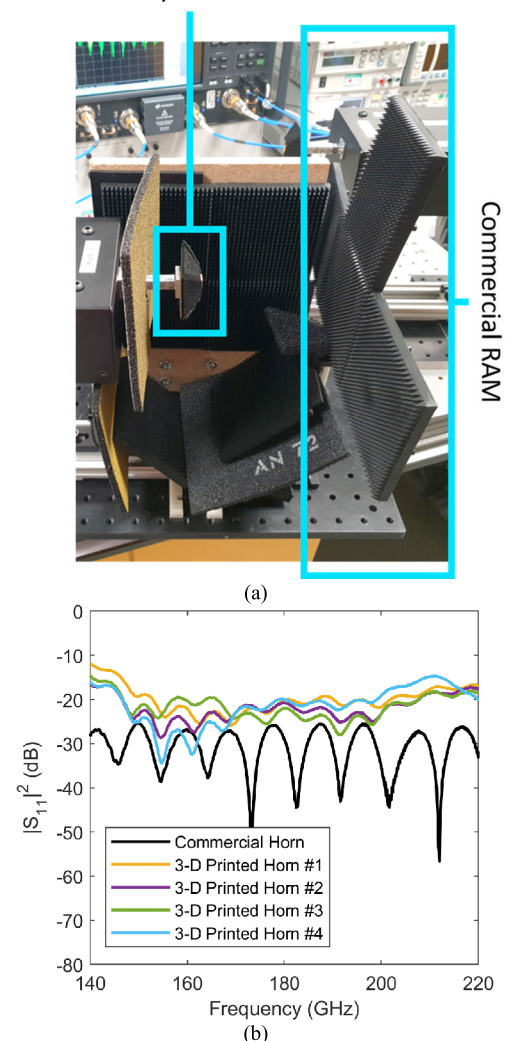

FIGURE 11. Reflection measurement setup and results for the rectangular horn antennas: (a) test setup showing the ruggedized 3-D printed modified replica antenna surrounded by commercial RAM; and (b) measured reflection coefficients for the commercial and replicated antennas.

The measured insertion loss between waveguide ports is shown in Fig. 12(b). Predictions are also included using textbook calculations for Friis transmission path loss, with quoted antenna gain values from 145 to 220 GHz [32]. It is important to note that the Friis transmission equation is only valid in the combined far-field for both antennas. As a result, the measured transmission loss can only be compared up to 194 GHz, corresponding to the combined far-field distance of 185 mm. Figure 12(b) shows approximately 0.5 dB difference between the measured trend and predictions. Note that while the low frequency Fabry-Pérot ripples are attributed to antenna flare length, the high frequency Fabry-Pérot ripples (with frequency periods of $\Delta f \sim 1.2, 1.4, 1.6$ GHz, ± 0.1 GHz) corresponds to the impedance mismatch reflections between both antennas. For example, between the smallest aperture size ($\Delta f \sim 1.4$ GHz gives $c/\Delta f \sim 214$ mm) and largest
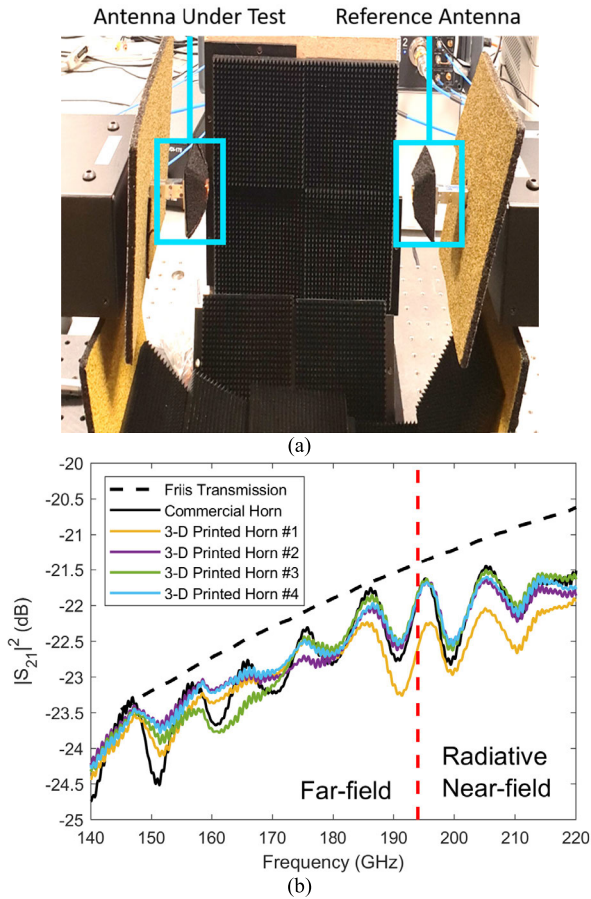
(a)

(b)

FIGURE 12. Transmission measurement setup and results for the rectangular horn antennas: (a) test setup showing the commercial horn antennas surrounded by commercial RAM; and (b) measured transmission coefficients for the commercial counterpart and replica antennas (1 GHz running averaged with 5 data points each side). The red dashed line shows the boundary between the far field and radiative near field.

aperture size ($\Delta f \sim 1.6$ GHz gives $c/\Delta f \sim 185$ mm) for the flares of both antennas. One possible explanation for $\Delta f \sim 1.2$ could be the very weak reflections between the RAM covering the metal boxes of both frequency extension heads ($c/\Delta f \sim 250$ mm).

Using the 'primary gain test method' with measured reference insertion loss $-10 \log_{10} |S_{21}|^2_R$, for the two identical commercial reference horn antennas, the reference boresight antenna gain G_R can be calculated by rearranging the Friis transmission path loss equation as [50]:

$$G_R = \left(\frac{4\pi R}{\lambda_0} \right) |S_{21}|_R \qquad (4)$$

From (4), the boresight gain for the 3-D printed horn antennas under test G_T can be determined using the Friis transmission path loss equation:

$$G_T = \left(\frac{4\pi R}{\lambda_0} \right)^2 \frac{|S_{21}|^2_T}{G_R} = \left(\frac{4\pi R}{\lambda_0} \right) \frac{|S_{21}|^2_T}{|S_{21}|_R} \qquad (5)$$
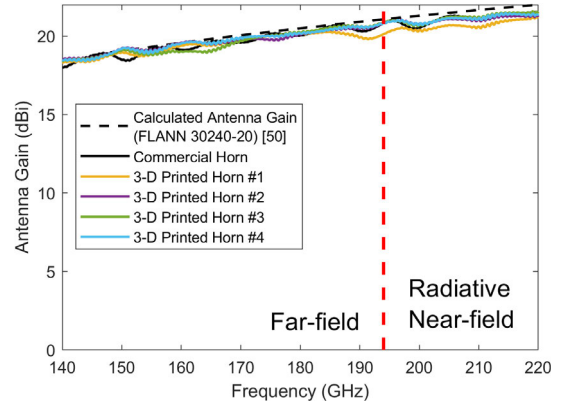

FIGURE 13. Extracted boresight antenna gains for the G-band commercial counterpart and ruggedized 3-D printed modified replica antennas. The red dashed line shows the boundary between the far field and radiative near field.
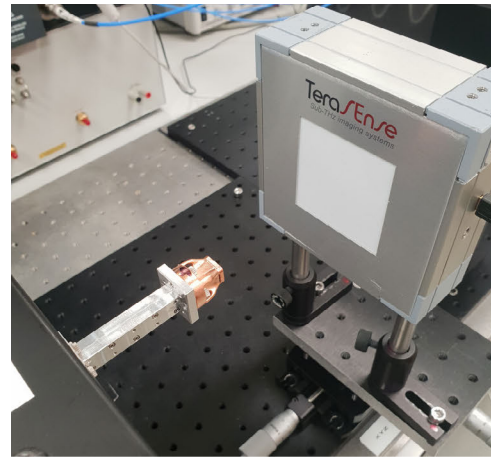

FIGURE 14. Measurement setup for spatial beam intensity profile imaging with 80 mm separation distance between antenna and camera apertures (commercial RAM is removed for this photograph).

where $-10 \log_{10} |S_{21}|^2_T$ is the insertion loss with both the antenna under test and the reference antenna. The extracted boresight gains for the antennas under test are shown in Fig. 13. The gain calculated by the manufacturer of the commercial horn antenna [32], using U.S. Naval Research Laboratory (NRL) Report 4433 (with accuracy of ± 0.3 dB) [50], is also included for comparison. Figure 13 shows only approximately 0.25 dB difference between the extracted trend and the quoted gains below 194 GHz.

In conclusion, all the 3-D printed modified replica horn antennas have comparable transmission performances with the commercial counterpart across the whole of G-band, again demonstrating excellent performance with this second test scenario.

To characterize the antenna beam profile within the far field, measurements are undertaken using the frequency extension heads (as a single-frequency source generator at 160 GHz) and the sub-THz imaging camera (having a peak in sensitivity at 160 GHz [45]), with its aperture located 80 cm from the antenna aperture, as shown in Fig. 14.

The TeraSense camera technology can perform qualitative measurements in real time. However, from our previous work
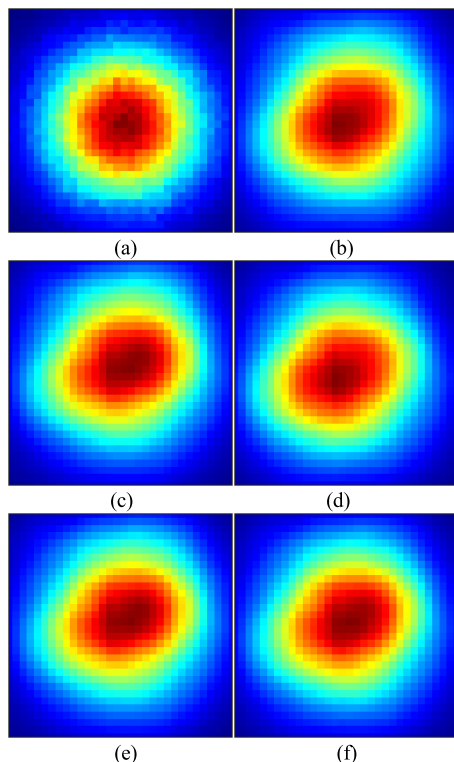
FIGURE 15. Measured normalized spatial beam intensity 2-D profiles for the G-band horn antennas with 80 mm separation distance between antenna and camera apertures: (a) HFSS simulation; (b) commercial horn; (c) Horn #1; (d) Horn #2; (e) Horn #3; and (f) Horn #4.

FIGURE 16. Cross-sectional beam intensity profiles for the G-band horn antennas extracted from Fig. 15: (a) E-field plane; and (b) H-field plane.

on benchmarking this camera [45], it was found that the Tera-1024 TeraSense camera exhibits limited image resolution and fidelity, with significant levels of systematic spatial noise (due to faulty pixels and high pixel-to-pixel responsivity deviation). Moreover, it was also found that the TeraSense camera (with additional RAM) has an inherent limitation with its relatively high reflectance (e.g., 27% at 79 GHz) aperture [45].

With any focal plane array (FPA), image quality is dependent on both spatial resolution and pixel fidelity. The latter is a function of the number and distribution of pixels that are faulty and those with large deviations in responsivity [45]. The TeraSense camera has a specified permissible number of faulty pixels of up to 3% and the specified pixel-to-pixel responsivity deviation from the mean value is within 20% [45].

Nevertheless, at 76 and 92 GHz, we previously showed that the spatial beam profile for a W-band rectangular horn antenna can be displayed by averaging-out pixel-related issues, using post image processing with the MATLAB 'disk smooth' filter [45]. For this reason, the same process is applied here.

The measured and post image processed spatial beam intensity 2-D profiles (normalized to their spatial peak intensity) for the commercial counterpart and ruggedized 3-D printed modified replica horn antennas are shown in Fig. 15(b) to (f). EM simulated results are also shown in Fig. 15(a), as a reference.
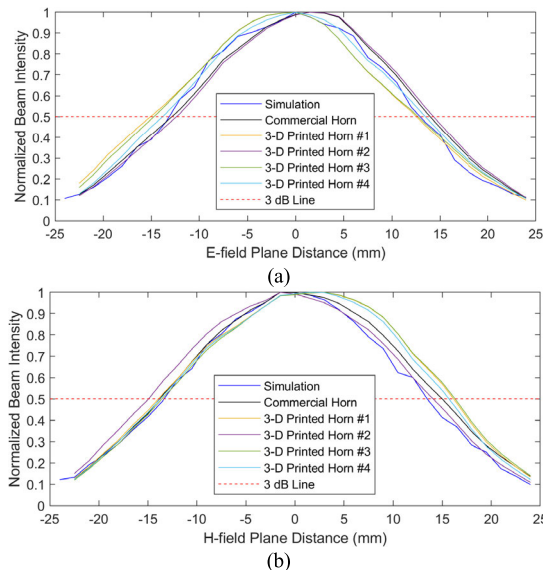
Figure 15 clearly shows that the beam profiles for the commercial counterpart and 3-D printed replica horn antennas have almost identical shapes and sizes. When compared to the circular EM simulated profile, all the measured profiles are slightly skewed. Possible reasons for this profile distortion include a combination of angular misalignment, pixel-related issues and/or standing waves [45].

Figure 16 shows the measured cross-sectional E- and H-field plane beam intensity profiles extracted from Fig. 15. It can be seen that the antenna-camera spatial alignment has shifted between each antenna measurement. It is believed that this may be a combination of small variations in torque applied to the screws holding the flanges together and slight movement in the frequency extension head. Nevertheless, it can be seen that all the E- and H-field plane beam intensity profiles for the 3-D printed antennas match both the commercial counterpart and the EM simulations very well, again demonstrating excellent performance with this third test scenario.

Table 4 gives the 3 dB beamwidths calculated and quoted by the manufacturer of the commercial horn antenna [32] and also our measured values extracted from Fig. 16. The difference between quoted and measured 3 dB beamwidths for E- and H-field planes are 0.1° and 1.6°, respectively, for the commercial horn antenna; the latter being relatively large, due to the skewed 2-D beam profiles. The worst-case differences in measured 3 dB beamwidths, between the modified replica and commercial counterpart antennas, are 0.6° and 0.9° for the E- and H- planes, respectively. Note that the small discrepancies in repeatability are due, in part, to the many limitations of the TeraSense camera (e.g., spatial resolution and pixel sensitivity); being difficult to accurately quantify.

In summary, from the measured performances of our ruggedized 3-D printed horn antennas, it can be concluded

TABLE 4. Extracted 3 dB beamwidths for the G-band horn antennas.

Horn Antennas	3 dB Beamwidth (°)	
	E-field Plane	H-field Plane
Calculated [32]	19.1	18.8
HFSS Simulation	18.5	19.1
Commercial Horn	19.0	20.4
3-D Printed Horn #1	19.6	21.3
3-D Printed Horn #2	19.4	20.5
3-D Printed Horn #3	19.5	21.2
3-D Printed Horn #4	19.3	20.8

that they have excellent mm-wave performance for replicating their commercial counterpart.

B. DIELECTRIC LENSES

The quoted maximum output power from the VDI WR-5.1 frequency extension head is only 6 dBm [51]. With the 90° OAPM, the two-sigma (i.e., $1/e^2$ normalized power) boundary for the collimated Gaussian beam (containing 95.45% of the beam power) projecting onto the TeraSense camera aperture cannot be determined, due to the poor signal-to-noise ratio at the FPA. Nevertheless, from simulations, the $1/e^2$ beamwidth is less than 50 mm and, as a result, our 60 mm diameter lenses are sufficiently large for this measurement.

To test the 3-D printed lenses, a lens holder and horn-mirror alignment frame are FDM 3-D printed, as shown in Fig. 17(a). Here, a commercial horn antenna and OAPM are employed. The collimated beam is focused by the lens and its focal point is found by moving the camera along the propagation *z*-axis, as shown in Fig. 17. It is important to note that this method is only qualitative, due to the dominant standing-wave between the TeraSense camera aperture and the lens [45].

With the conventional hyperbolic aspherical plano-convex lens, the approximate focal length is 73 mm, which is close to the designed value of 76.2 mm. The associated focused beam spot image is shown in Fig. 17(b). Here, only one pixel displays the unity value of normalized intensity (shown as a red pixel). The pitch of the pixels in the FPA is 1.5 mm, while the size of each individual detector within each pixel area is unknown. For this reason, it is not possible to determine the exact spot size.

With the Fresnel lens, the approximate focal length is 61 mm and the corresponding focused beam spot image is shown in Fig. 17(c). Again, only one pixel displays the unity value of normalized intensity (shown as a red pixel). The deviation in focal length, from its designed value of 76.2 mm, is much bigger with the Fresnel lens. Possible reasons for this are the non-optimized design and significant warpage. Nevertheless, both ultra-low cost lenses demonstrate their capability for focusing a collimating quasi-optical beam.

V. G-BAND MIRROR, POLARIZER AND RAM MEASUREMENTS

The 3-D printed quasi-optical housing is utilized to evaluate the performances of the 90° OAPM, grid polarizer and
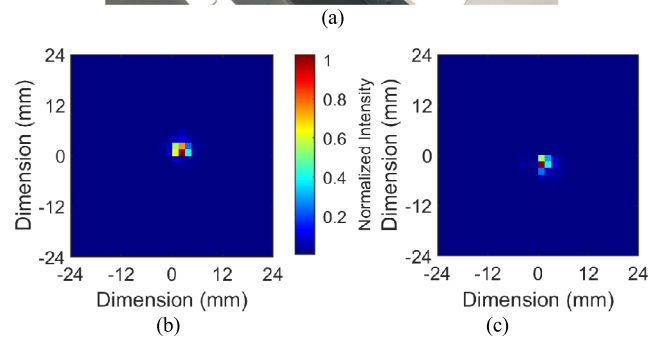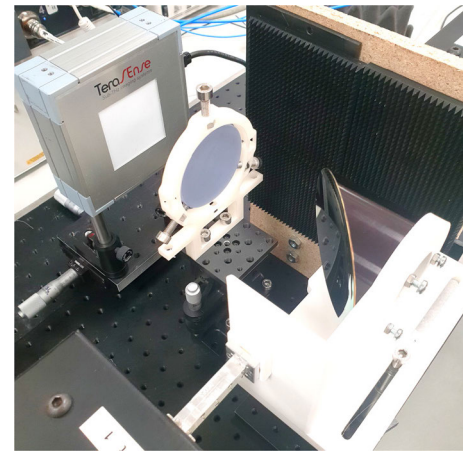

FIGURE 17. Measured spatial beam intensity 2-D profile images for the hyperbolic aspherical plano-convex lenses: (a) measurement setup; (b) conventional lens focal point image; and (c) Fresnel lens focal point image.

RAM. The 'plug and play' housing can accommodate a mixture of commercial and 3-D printed components and their configurations, as a quasi-optical subsystem assembly. Figure 18(a) illustrates a typical configuration for our quasi-optical housing. Custom-built 3-D printed mechanical interface adapters are used between the horn antennas and housing. Photographs for the complete integrated subsystem assembly are shown in: (i) Fig. 6, using commercial antennas and mirrors; (ii) Fig. 18(b), using all 3-D printed quasi-optical components (antennas, mirrors, RAM and polarizer).

A. PARABOLIC MIRRORS

As a reference, to evaluate the performance of the 3-D printed 90° OAPMs, the housing is first assembled using all commercial antennas and mirrors (without the rotating platform). The commercial mirror at Mirror Position 1 is replaced with its mass-reduced 3-D printed modified replica. The measured insertion loss for the commercial counterpart and its replica mirrors is shown on Fig. 19. It can be seen that all the 3-D printed mirrors have excellent performances, with measured port-to-port insertion loss between 2.0 to 3.5 dB across G-band. By comparison, the National Metrology Institute of Germany, Physikalisch-Technische Bundesanstalt (PTB), reported an insertion loss better than 4 dB, between 50 GHz and 325 GHz, using identical commercial components and
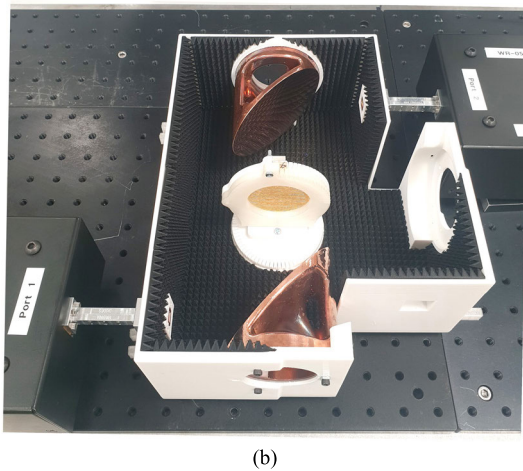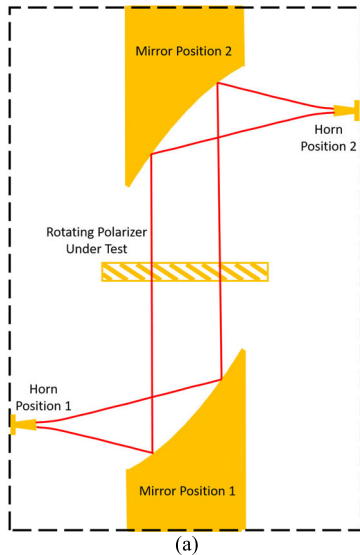
S.-H. Shin *et al.*: Polymer-Based 3-D Printed 140-220 GHz Low-Cost Quasi-Optical Components and Integrated Subsystem Assembly

IEEE *Access*

(a)

(b)

FIGURE 18. Typical configuration for our 3-D printed quasi-optical housing with HMMH arrangement having the two OAPMs rotated 180° about their common optical axis and the central two-axis rotating platform containing the grid polarizer under test: (a) illustration; (b) corresponding photograph of the complete integrated subsystem assembly realized using all 3-D printed quasi-optical components (antennas, mirrors, RAM and polarizer).

their custom-machined mechanical alignment rig (90° rotated mirror mounting) [52], [53]. This clearly shows that our 3-D printed quasi-optical housing offers very accurate spatial alignment over the complete subsystem assembly, having a total port-to-port path length of 356 mm (corresponding to $166\lambda_0(140$ GHz$)$). Moreover, there is no noticeable difference in measurements between commercial counterpart and mass-reduced 3-D printed modified replica mirrors, which shows our choice of 3-D printing technologies (FDM for the housing and SLA for the mirrors) provides excellent dimensional accuracy for their intended purpose.

In addition, to evaluate the quasi-optical subsystem assembly employing either all commercial counterpart antennas and mirrors (Fig. 6, without the rotating platform) or all 3-D printed modified replicas (Fig. 18(b), without the rotating platform), the S-parameter measurements for both scenarios
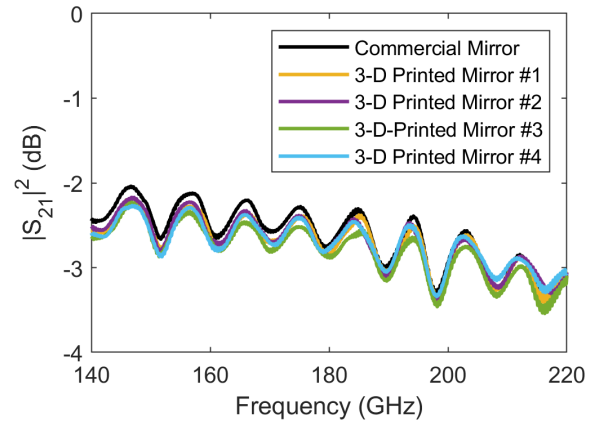

FIGURE 19. Measured port-to-port transmission coefficients for the commercial counterpart and mass-reduced 3-D printed modified replica 90° OAPMs (2 GHz running averaged with 10 data points each side).
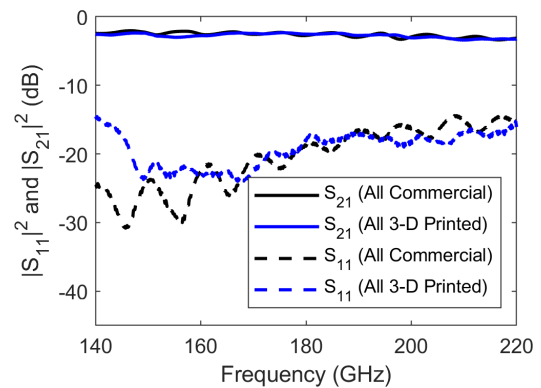

FIGURE 20. Measured S-parameters for the quasi-optical subsystem assembly employing either all commercial counterpart antennas and mirrors or all 3-D printed modified replicas, over a path length of 356 mm (2 GHz running averaged with 10 data points each side).

are shown in Fig. 20. It can be seen that the all 3-D printed subsystem shows excellent performance. This clearly demonstrates that a complete quasi-optical subsystem can be entirely manufactured out of 3-D printed components, without significantly sacrificing performance, at G-band.

B. GRID POLARIZER

To evaluate the 3-D printed grid polarizer, the housing is fitted with the rotating platform (having 3-D printed alignment markers at every 5° intervals of rotation) and only commercial antennas and mirrors are employed. Figure 6 shows the *in-situ* measurement setup of our linear polarizer.

The embedded polarizer subsystem (denoted by subscript $p-s$) S-parameter measurements S_{11p-s} and S_{21p-s} are recorded for every 5° of polarizer rotation angle θ_p, ranging from 0° (horizontal grid lines) to 90° (vertical grid lines). With the vertically polarized rectangular horn antennas, at 160 GHz, the insertion loss is at a minimum with $\theta_p = 0$ and maximum with $\theta_p = 70°$ (and not at the expected 90°, possibly due to stress-induced mechanical distortion of the grid), as shown in Fig. 21(a). At 160 GHz, Fig. 21(b) shows
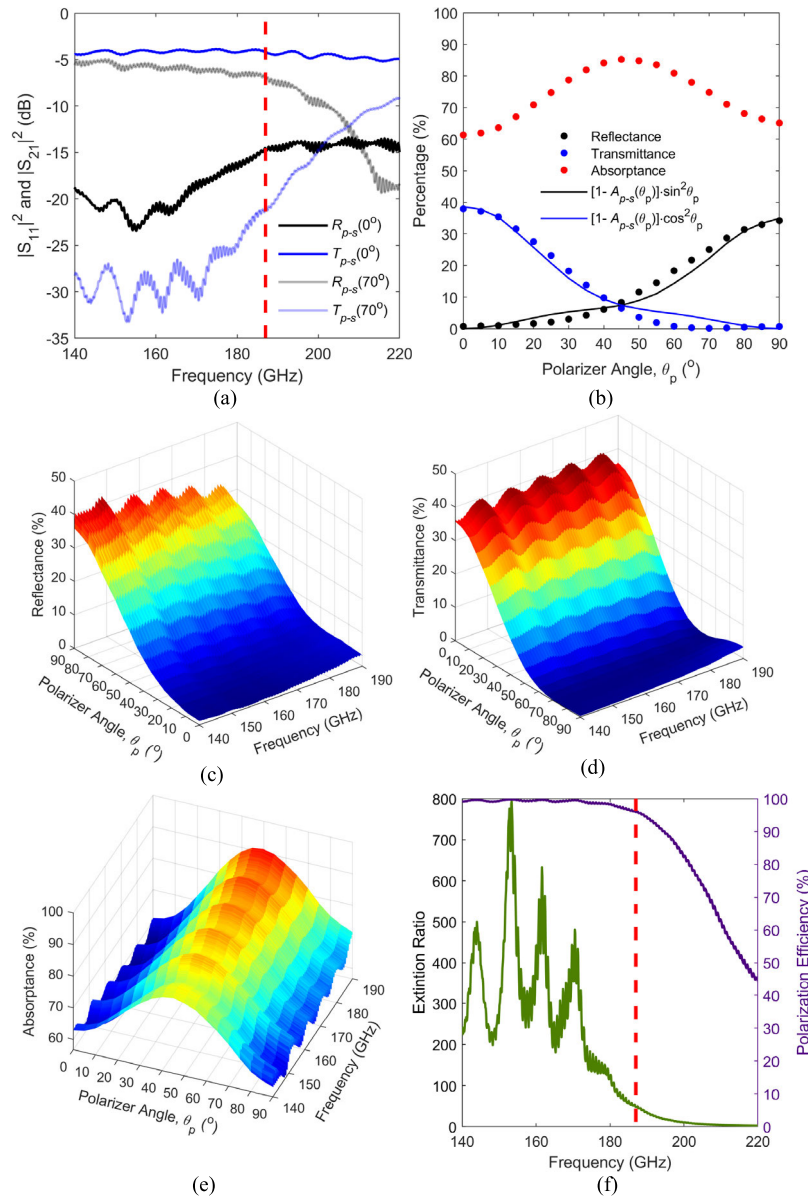
IEEE *Access*

S.-H. Shin *et al.*: Polymer-Based 3-D Printed 140-220 GHz Low-Cost Quasi-Optical Components and Integrated Subsystem Assembly

FIGURE 21. Measurement results for the grid polarizer: (a) embedded S-parameters, with transmittance $T_{p-s}(\theta_p)$ (dB) in blue and reflectance $R_{p-s}(\theta_p)$ (dB) in black – darker and lighter colours are for 0° and 70° polarizer angles, respectively; (b) embedded polarizer power reflectance, transmittance and absorptance against polarizer angle at 160 GHz; embedded polarizer angle-frequency surface plot for (c) reflectance, (d) transmittance and (e) absorptance; and (f) polarization efficiency and extinction ratio performance. In (a) to (f), there is a 2 GHz running averaged with 10 data points each side and the red dashed line shows the TE upper cut-off frequency.

the measured rotation angle dependency for the embedded polarizer power reflectance $R_{p-s}(\theta_p) = |S_{11p-s}(\theta_p)|^2 \xrightarrow{lossless} \sin^2\theta_p$, transmittance $T_{p-s}(\theta_p) = |S_{21p-s}(\theta_p)|^2 \xrightarrow{lossless} \cos^2\theta_p$ and absorptance [54] (also known as power loss factor):

$$A_{p-s}(\theta_p) = 1 - |S_{11p-s}(\theta_p)|^2 - |S_{21p-s}(\theta_p)|^2 \quad (6)$$

Using the principle of conservation of energy, given in (6), the solid lines in Fig. 21(b) show the semi-analytical

modeling for power reflectance and transmittance, based on the extracted absorptance.

The respective polarizer angle-frequency surface plots for power reflectance, transmittance and absorptance are shown in Fig. 21(c), (d) and (e).

The embedded absorptance (for the complete subsystem assembly) is between 57% and 90%, from 140 to 187 GHz, indicating poor power efficiency due to ohmic and radiative (diffraction) losses. In practice, the de-embedded absorptance will be better. Since $|S_{21p-s}|^2$ includes the insertion

S.-H. Shin *et al.*: Polymer-Based 3-D Printed 140-220 GHz Low-Cost Quasi-Optical Components and Integrated Subsystem Assembly

IEEE *Access*

loss of the quasi-optical housing (without the polarizer), the de-embedded polarizer power transmittance T_p can be approximated using power propagation modeling [54] from:

$$T_p(\theta_p) \simeq \frac{|S_{21p-s}(\theta_p)|^2}{|S_{21}|^2} \tag{7}$$

where $|S_{21}|^2$ is the measured insertion loss of the quasi-optical housing without the polarizer, given by the solid black line in Fig. 20. The degree of polarization (or polarization efficiency) P and extinction ratio E_p are calculated from:

$$P = \frac{E_p - 1}{E_p + 1} \text{ and } E_p = \frac{T_p(0°)}{T_p(70°)} \approx \frac{|S_{21p-s}(0°)|^2}{|S_{21p-s}(70°)|^2} \tag{8}$$

The polarization efficiency and extinction ratio, across G-band, are shown in Fig. 21(f). With our 3-D printed design, the theoretical TE upper cut-off frequency is 187 GHz. At this frequency, the polarization efficiency and extinction ratio are 96% and 48, respectively. From 140 to 180 GHz, these respective values are better than 98% and 118. This compares favorably with commercial free-standing wire grid polarizers, used for ultra-broadband (sub-)millimeter-wave applications, having low to medium values of extinction ratio when to compared to other polarizer technologies. For example, the PW010-040-050 (from PureWavePolarizers Ltd., U.K.) is a 50 mm diameter (34 mm aperture) grid polarizer that uses 10 μm diameter tungsten wires, spaced 40 μm apart and, at 150 GHz, has normalized power transmittance values of $\bar{T}_p(0°) \simeq 99.9\%$ and $\bar{T}_p(90°) \simeq 0.3\%$, respectively [55]; giving polarization efficiency and extinction ratio values of 99.4% and $E_p \approx 333$ at 150 GHz.

Note that the in-band high frequency Fabry-Pérot ripples, seen in Fig. 21(a) and (f), (with frequency period $\Delta f \sim$ 1.7 GHz) correspond to reflections between the grid polarizer and both antenna apertures ($c/\Delta f \sim 178$ mm).

The results show that with a low-cost FDM 3-D printer, even with its poor resolution, a usable grid polarizer can be fabricated. Moreover, while this first non-optimized proof-of-principle demonstrator exhibits poor power efficiency, it performs its primary function with sufficient extinction ratio below its 187 GHz TE upper cut-off frequency.

C. RADIATION ABSORBENT MATERIAL

To evaluate the performance of our 3-D printed RAM, we placed a tile against a flat copper back plate and illuminated it at normal incidence with a collimated beam. The RAM tile and back plate are mounted on the rotational platform within the 3-D printed quasi-optical housing, as shown in Fig. 22(a). It is important to note that the commercial horn antenna used is not ideal, having a finite return loss. As a result, the dynamic range for this measurement scenario is limited by the performance of the commercial horn antenna.

The measured return loss for the copper back plate and 3-D printed RAM (against the copper back plate) are shown in Fig. 22(b). With the former, the back plate reflects most of the power, and the resulting G-band average return loss is
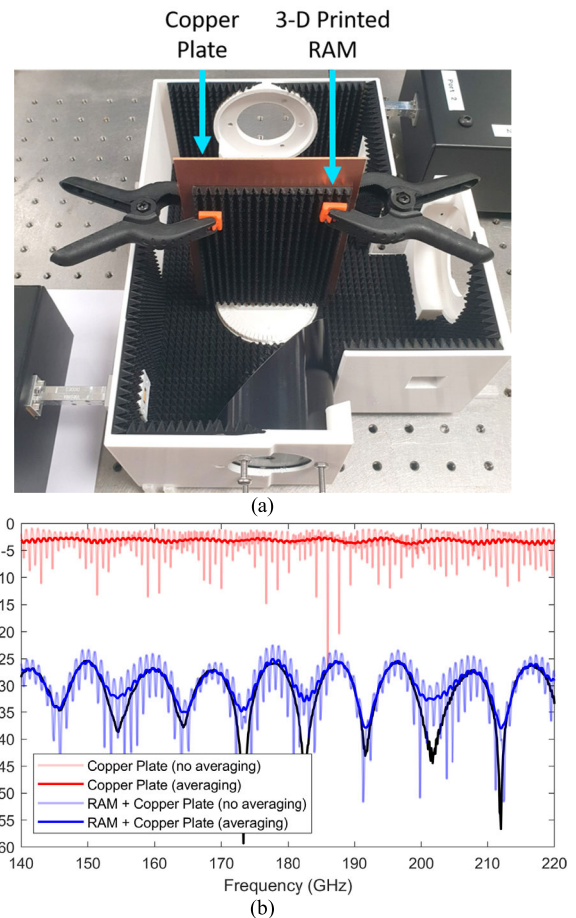

FIGURE 22. Measurement of the 3-D printed RAM (with copper back plate) exposed to a collimated beam at normal incidence: (a) test setup with commercial horn and mirror; (b) reflection coefficients (commercial horn measurement from Fig. 11 is shown by the black curve). With the darker lines there is a 1 GHz running averaged with 5 data points each side.

2.98 dB. With a perfect lossless system, the return loss from the back plate should be 0 dB. However, our band-average return loss is consistent (within 0.37 dB) with our previous port-to-port measurement for the horn-mirror-mirror-horn insertion loss of 2.61 dB. When RAM is added, the return loss decreases below 25 dB, which is near the lower end of the dynamic range limitation for our scenario. This clearly shows that the 3-D printed RAM is capable of suppressing normal incidence reflections (i.e., two-way transmission through the RAM) by at least 21 dB. While absorption is the primary mechanism for this high value of suppression, scattering will also contribute to some degree. Note that, the high frequency Fabry-Pérot ripples correspond to the weak reflections between the RAM-covered copper back plate and the antenna; the amplitude of these ripples will reduce with an increase in the base thickness of the RAM.

To observe the performance of the RAM for a diverging incident beam, a tile is placed mid-way between commercial horn antennas, facing one another, as shown in Fig. 23(a). The antenna at Port 2 is facing the front pyramidal side of the
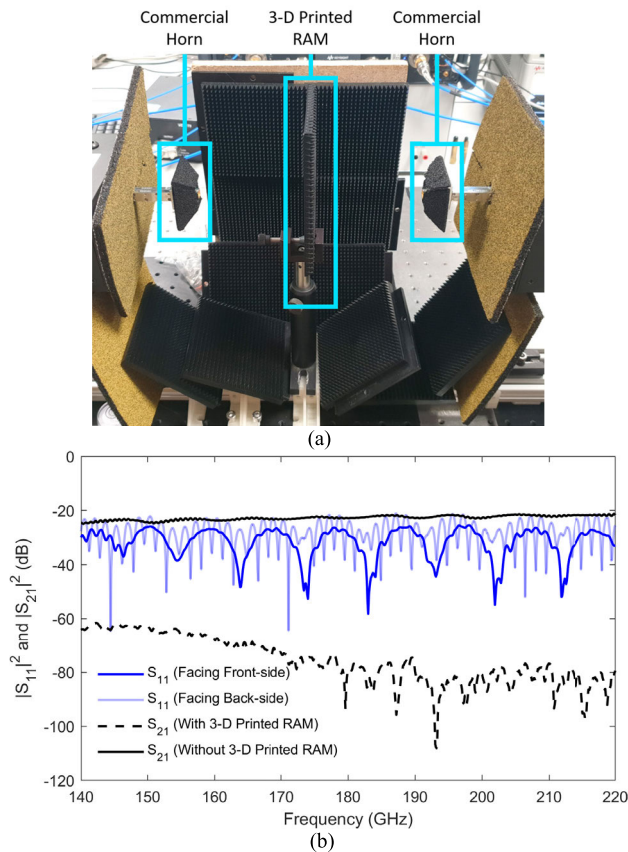
FIGURE 23. Horn-RAM-horn measurements (no averaging) with 3-D printed RAM (without copper back plate) inserted mid-way between antennas: (a) test setup with commercial horn antennas; (b) S-parameters.

RAM, while the antenna at Port 1 is facing the back flat side of the RAM, with measured return loss for both ports shown in Fig. 23(b).

Figure 23(b) shows that without the RAM, the worst-case insertion loss is approximately 23 dB. When the RAM is added, the worst-case insertion loss is 60 dB. This clearly shows that adding the 3-D printed RAM provides better than 37 dB of isolation. In addition, as expected, the pyramidal front side of the RAM reduces reflections more than the flat backside. With the former, the dominant low frequency Fabry-Pérot ripples are attributed to the illuminating antenna itself. With the latter, the high frequency Fabry-Pérot ripples (with frequency period $\Delta f \sim 3.2$ GHz) corresponds to the distance between the backside of the RAM and the antenna ($c/\Delta f \sim 88.5$ mm). This clearly indicates that the wave impedance transforming gradient, with our tessellating pyramidal array on the front side, allows the FDM 3-D printed RAM to be highly effective across the whole of G-band.

VI. CONCLUSION

This paper first gives a literature review of the current state-of-the-art in polymer-based 3-D printing technologies for quasi-optical applications at upper-mm-wave frequencies. It is found that few examples of individual component types

have been previously demonstrated above *ca.* 100 GHz, with most being reported within the past five years. With reference to the papers cited in the open literature, we demonstrate the art-of-the-possible in G-band by using low-cost 3-D printing, normally associated with microwave frequencies and longer wavelength applications.

Five different quasi-optical component types are investigated; antennas, mirrors, RAM, polarizers and lenses. As an alternative to conventional electroplating, gold-leaf gilding is used for the polarizer. A detailed investigation is undertaken to compare the performance of our 3-D printed horn antenna, parabolic mirror and RAM with their commercial equivalents; demonstrating comparable performances. Although our FDM 3-D printed grid polarizer is limited by the minimum strip width, separation distance and metallization thickness, it shows potential for further development using a smaller nozzle or different 3-D printer technology (e.g., MSLA, SLA, RECILS). The hyperbolic aspherical plano-convex lenses both demonstrated their focusing ability. All the antennas and lenses are fabricated using one of the lowest cost 3-D printing technologies (MSLA) available on the open market.

In addition, a fully 3-D printed, RAM-lined housing with central two-axis rotational platform is constructed. This ultra-low cost, 'plug and play' housing is design to give a fast measurement setup, while minimizing misaligning losses. Its RAM lining is designed to suppress reflections due to diffraction from components under test that may cause adverse multi-path interference. Using this housing, we demonstrate accurate two-port quasi-optical measurements; for example, an integrated horn-mirror-polarizer-mirror-horn subsystem assembly.

While being constrained by the current 3-D printing technologies accessible to the authors, our work opens-up new opportunities for rapid prototyping of complete low-cost, high performance quasi-optical upper-mm-wave subsystems. Indeed, with the continual advancements in all aspects of affordable 3-D printers, and their materials, better resolution and higher performance can be expected in the near future.

REFERENCES
[1] M. D'Auria, W. J. Otter, J. Hazell, B. T. W. Gillatt, C. Long-Collins, N. M. Ridler, and S. Lucyszyn, "3-D printed metal-pipe rectangular waveguides," *IEEE Trans. Compon., Packag., Manuf. Technol.*, vol. 5, no. 9, pp. 1339–1349, Sep. 2015.

[2] S.-H. Shin, D. F. Alyasiri, M. D'Auria, W. J. Otter, C. W. Myant, D. Stokes, Z. Tian, N. M. Ridler, and S. Lucyszyn, "Polymer-based 3-D printed ku-band steerable phased-array antenna subsystem," *IEEE Access*, vol. 7, pp. 106662–106673, Aug. 2019.

[3] E. Márquez-Segura, W. J. Otter, S. Lucyszyn, and N. Ridler, "Fabricación aditiva de atenuadores variables de veleta rotatoria en guía de onda," in *Proc. 34th Simposium Nacional de la Unión Científica Internacional de Radio (URSI)*, Seville, Spain, Sep. 2019.

S.-H. Shin *et al.*: Polymer-Based 3-D Printed 140-220 GHz Low-Cost Quasi-Optical Components and Integrated Subsystem Assembly

IEEE *Access*

[4] W. J. Otter and S. Lucyszyn, "Hybrid 3-D-printing technology for tunable THz applications," *Proc. IEEE*, vol. 105, no. 4, pp. 756–767, Apr. 2017.

[5] W. J. Otter, N. M. Ridler, H. Yasukochi, K. Soeda, K. Konishi, J. Yumoto, M. Kuwata-Gonokami, and S. Lucyszyn, "3D printed 1.1 THz waveguides," *Electron. Lett.*, vol. 53, no. 7, pp. 471–473, Mar. 2017.

[6] S. Lucyszyn, X. Shang, W. J. Otter, C. Myant, R. Cheng, and N. M. Ridler, "Polymer-based 3D printed millimeter-wave components for spacecraft payloads," in *Proc. IEEE MTT-S Int. Microw. Workshop Adv. Mater. Processes (IMWS-AMP)*, Ann Arbor, MI, USA, Jul. 2018, pp. 1–3.

[7] B. Zhang, P. Linner, C. Karnfelt, P. L. Tarn, U. Sodervall, and H. Zirath, "Attempt of the metallic 3D printing technology for millimeter-wave antenna implementations," in *Proc. Asia–Pacific Microw. Conf. (APMC)*, Nanjing, China, Dec. 2015, pp. 1–3.

[8] B. Zhang, Z. Zhan, Y. Cao, H. Gulan, P. Linner, J. Sun, T. Zwick, and H. Zirath, "Metallic 3-D printed antennas for millimeter- and submillimeter wave applications," *IEEE Trans. THz Sci. Technol.*, vol. 6, no. 4, pp. 592–600, Jul. 2016.

[9] P. T. Timbie, J. Grade, D. van der Weide, B. Maffei, and G. Pisano, "Stereolithographed mm-Wave corrugated horn antennas," in *Proc. Int. Conf. Infr., Millim., THz Waves*, Houston, TX, USA, Oct. 2011, pp. 1–3.

[10] E. Decrossas, T. Reck, C. Lee, C. Jung-Kubiak, I. Mehdi, and G. Chattopadhyay, "Evaluation of 3D printing technology for corrugated horn antenna manufacturing," in *Proc. IEEE Int. Symp. Electromagn. Compat. (EMC)*, Ottawa, Canada, Jul. 2016, pp. 251–255.

[11] A. Macor, E. de Rijk, S. Alberti, T. Goodman, and J.-P. Ansermet, "Note: Three-dimensional stereolithography for millimeter wave and terahertz applications," *Rev. Sci. Instrum.*, vol. 83, no. 4, Apr. 2012, Art. no. 046103.

[12] A. von Bieren, E. de Rijk, J.-P. Ansermet, and A. Macor, "Monolithic metal-coated plastic components for mm-Wave applications," in *Proc. 39th Int. Conf. Infr., Millim., THz Waves (IRMMW-THz)*, Tuscon, AZ, USA, Sep. 2014, pp. 1–2.

[13] A. Molaei, A. Bisulco, L. Tirado, A. Zhu, D. Cachay, A. G. Dagheyan, and J. M-Lorenzo, "3-D-printed E-band compressive horn antenna for high-sensing-capacity imaging applications," in *Proc. IEEE Antennas Wireless Propag. Lett.*, vol. 17, no. 9, pp. 1639–1642, Sep. 2018.

[14] A. Jammes, E. des Gayets, K. Staelens, R. Feger, T. Lampersberger, and A. Stelzer, "Silver metallization of 77 GHz 3D printed horn antennas," in *Proc. 12th Eur. Conf. Antennas Propag. (EuCAP)*, London, U.K., Apr. 2018, pp. 1–4.

[15] J. Romeu, S. Blanch, N. Vidal, J. M. Lopez-Villegas, and A. Aguasca, "Assessment of 3-D printing technologies for millimeter-wave reflectors," *IEEE Antennas Wireless Propag. Lett.*, vol. 17, no. 11, pp. 2061–2064, Nov. 2018.

[16] D. B. Fullager, S. Park, C. Hovis, Y. Li, J. Reese, E. Sharma, S. Lee, C. Evans, G. D. Boreman, and T. Hofmann, "Metalized poly-methacrylate off-axis parabolic mirrors for terahertz imaging fabricated by additive manufacturing," *J. Infr., Millim., THz Waves*, vol. 40, no. 3, pp. 269–275, Jan. 2019.

[17] Form 3. (2020). *Formlabs*. Accessed: Dec. 24, 2020. [Online]. Available: https://formlabs.com/uk/3d-printers/form-3/

[18] E. Huber, M. Mirzaee, J. Bjorgaard, M. Hoyack, S. Noghanian, and I. Chang, "Dielectric property measurement of PLA," in *Proc. IEEE Int. Conf. Electro Inf. Technol. (EIT)*, Grand Forks, ND, USA, May 2016, pp. 788–792.

[19] K. G. Kjelgard, D. T. Wisland, and T. S. Lande, "3D printed wideband microwave absorbers using composite graphite/PLA filament," in *Proc. 48th Eur. Microw. Conf. (EuMC)*, Sep. 2018, pp. 859–862.

[20] Conductive PLA. *Proto-Pasta*. Accessed: Dec. 24, 2020. [Online]. Available: https://www.proto-pasta.com/pages/conductive-pla.

[21] Y. Arbaoui, V. Laur, A. Maalouf, P. Quéfféelec, D. Passerieux, A. Delias, and P. Blondy, "Full 3-D printed microwave termination: A simple and low-cost solution," *IEEE Trans. Microw. Theory Techn.*, vol. 64, no. 1, pp. 271–278, Jan. 2016.

[22] M. Petroff, J. Appel, K. Rostem, C. L. Bennett, J. Eimer, T. Marriage, J. Ramirez, and E. J. Wollack, "A 3D-printed broadband millimeter wave absorber," *Rev. Sci. Instrum.*, vol. 90, no. 2, Feb. 2019, Art. no. 024701.

[23] A. I. Hernandez-Serrano, Q. Sun, E. G. Bishop, E. R. Griffiths, C. P. Purssell, S. J. Leigh, J. Lloyd-Hughes, and E. Pickwell-MacPherson, "Design and fabrication of 3-D printed conductive polymer structures for THz polarization control," *Opt. Exp.*, vol. 27, no. 8, pp. 11635–11641, Apr. 2019.

[24] M. Ryu, D. Linklater, W. Hart, A. Balytis, E. Skliutas, M. Malinauskas, D. Appadoo, Y.-R. E. Tan, E. P. Ivanova, J. Morikawa, and S. Juodkazis, "3D printed polarizing grids for IR-THz synchrotron radiation," *J. Opt.*, vol. 20, no. 3, pp. 1–7, Jan. 2018.

[25] H. Yi, S.-W. Qu, K.-B. Ng, C. H. Chan, and X. Bai, "3-D printed millimeter-wave and terahertz lenses with fixed and frequency scanned beam," *IEEE Trans. Antennas Propag.*, vol. 64, no. 2, pp. 442–449, Feb. 2016.

[26] N. Chudpooti, N. Duangrit, P. Akkaraekthalin, I. D. Robertson, and N. Somjit, "220-320 GHz hemispherical lens antennas using digital light processed photopolymers," *IEEE Access*, vol. 7, pp. 12283–12290, Jan. 2019.

[27] A. D. Squires, E. Constable, and R. A. Lewis, "3D printed terahertz diffraction gratings and lenses," *J. Infr., Millim., THz Waves*, vol. 36, no. 1, pp. 72–80, Jan. 2015.

[28] R. J. Friel, M. Gerling-Gerdin, E. Nilsson, and B. P. Andreasson, "3D printed radar lenses with anti-reflective structures," *Designs*, vol. 3, no. 2, 28, pp. 1–11, Jun. 2019.

[29] A. C. Paolella, C. D. Fisher, C. Corey, D. Foster, and D. Silva-Saez, "3-D printed millimeter-wave lens systems at 39 GHz," *IEEE Microw. Wireless Compon. Lett.*, vol. 28, no. 6, pp. 464–466, Jun. 2018.

[30] C. D. Fisher, A. C. Paolella, C. Corey, D. Foster, and D. Silva-Saez, "3-D printed millimeter wave quasi-optical lens system for 60 and 100 GHz applications," in *Proc. IEEE Radio Wireless Symp. (RWS)*, Orlando, FL, USA, Jan. 2019, pp. 1–3.

[31] A. C. Paolella, C. Corey, D. Foster, J. Desjardins, C. Smith, and L. Walters, "Broadband millimeter wave characterization of 3-D printed materials," in *IEEE MTT-S Int. Microw. Symp. Dig.*, Philadelphia, PA, USA, Jun. 2018, pp. 1565–1568.

[32] *Calibration Certificates RISE Equipment Used for Test Report 2P03617*. Accessed: Dec. 24, 2020. [Online]. Available: https://fccid.io/TA8AKRX10102/Test-Report/Equipment-certificates-4745782/ViewExhibitReport.cfm

[33] *IEEE Standard for Rectangular Metallic Waveguides and Their Interfaces for Frequencies of 110 GHz and Above—Part 1: Frequency Bands and Waveguide Dimensions*, IEEE Standard 1785.1-2012, 2012.

[34] *IEEE Standard for Rectangular Metallic Waveguides and Their Interfaces for Frequencies of 110 GHz and Above—Part 2: Waveguide Interfaces*, IEEE Standard 1785.2-2016, 2016.

[35] *Edmund Optics Ltd Datasheet for 76.2 x 38.1 mm PFL 90 Degree Off-Axis Parabolic Aluminum Mirror*. Accessed: Dec. 24, 2020. [Online]. Available: https://www.edmundoptics.co.uk/p/762-x-381mm-pfl-90-off-axis-parabolic-aluminum-mirror/33594/

[36] C. Brückner, G. Notni, and A. Tünnermann, "Optimal arrangement of 90 off-axis parabolic mirrors in THz setups," *Optik*, vol. 121, no. 1, pp. 113–119, Jan. 2010.

[37] Y. Wang, X. Shang, N. M. Ridler, M. Naftaly, A. I. Dimitriadis, T. Huang, and W. Wu, "Material measurements using VNA-based material characterization kits subject to thru-reflect-line calibration," *IEEE Trans. THz Sci. Technol.*, vol. 10, no. 5, pp. 466–473, Sep. 2020.

[38] Elegoo Mars (2020). *Elegoo*. Accessed: Dec. 24, 2020. [Online]. Available: https://www.elegoo.com/products/elegoo-mars-pro-lcd-3d-printer.

[39] Chitubox. (2020). *Chtubox*. Accessed: Dec. 24, 2020. [Online]. Available: https://www.chitubox.com/en

[40] PreForm. (2020). *Formlabs*. Accessed: Dec. 24, 2020. [Online]. Available: https://formlabs.com/uk/software/

[41] Raise Pro2 (2019). *Raise3D*. Accessed: Dec. 24, 2020. [Online]. Available: https://www.raise3d.com/pro2/

[42] IdeaMaker. (2019). *Raise3D*. Accessed: Dec. 24, 2020. [Online]. Available: https://www.raise3d.com/ideamaker/

[43] MG Chemicals. *842AR Technical Data Sheet*. Accessed: Dec. 24, 2020. [Online]. Available: https://www.mgchemicals.com/products/conductive-paint/conductive-acrylic-paints/silver-conductive-paint/.

[44] N. Shoaib, N. M. Ridler, and M. J. Salter, "Commissioning of the NPL WR-05 waveguide network analyser system for S-parameter measurements from 140 GHz to 220 GHz," Nat. Phys. Lab., Teddington, U.K., NPL Rep. TQE 12, Mar. 2015.

[45] S.-H. Shin and S. Lucyszyn, "Benchmarking a commercial (sub-)THz focal plane array against a custom-built millimeter-wave single-pixel camera," *IEEE Access*, vol. 8, pp. 191174–191190, Oct. 2020.

[46] A. Lonnqvist, A. Tamminen, J. Mallat, and A. V. Raisanen, "Monostatic reflectivity measurement of radar absorbing materials at 310 GHz," *IEEE Trans. Microw. Theory Techn.*, vol. 54, no. 9, pp. 3486–3491, Sep. 2006.

IEEE *Access*

S.-H. Shin *et al.*: Polymer-Based 3-D Printed 140-220 GHz Low-Cost Quasi-Optical Components and Integrated Subsystem Assembly

[47] TK Instruments. *Space Qualified Tessellating TeraHertz RAMs for the 50 to 1000 GHz Region and Beyond*. Accessed: Dec. 24, 2020. [Online]. Available:http://www.terahertz.co.uk/index.php?option=com_content&view=article&id=145&Itemid=448

[48] TK Instruments. *Thomas Keating and QMC Instruments: Space Capabilities*. Accessed: Dec. 24, 2020. [Online]. [Online]. Available: http://www.terahertz.co.uk/images/tki/brochures/TK_Space_experience_2013-04-16a.pdf

[49] *ECCOSORB AN Flexible Foam Sheet Broadband Microwave Absorber*. Accessed: Dec. 24, 2020. [Online]. [Online]. Available: https://www.laird.com/sites/default/files/eccosorb-an-datasheet.pdf

[50] W. T. Slayton, "Design and calibration of microwave antenna gain standards," Nav. Res. Lab., Washington, DC, USA, Tech. Rep. 4433, Nov. 1954.

[51] *VNA Extender—VDI Model: WR5.1-VNAX. VDI*. Accessed: Dec. 24, 2020. [Online]. Available: https://www.vadiodes.com/index.php/en/products/vector-network-analyzer?id=853

[52] A. Kazemipour, M. Hudlicka, S.-K. Yee, M. A. Salhi, D. Allal, T. Kleine-Ostmann, and T. Schrader, "Design and calibration of a compact quasi-optical system for material characterization in millimeter/submillimeter wave domain," *IEEE Trans. Instrum. Meas.*, vol. 64, no. 6, pp. 1438–1445, Jun. 2015.

[53] A. Kazemipour, M. Salhi, T. Kleine-Ostmann, and T. Schrader, "Design and calibration of a compact quasi-optical system for material characterization in millimeter/submillimeter wave domain," in *Proc. THz Secur. Sci. Workshop*, Davos, Switzerland, May 2015.

[54] J. Sun and S. Lucyszyn, "Extracting complex dielectric properties from reflection-transmission mode spectroscopy," *IEEE Access*, vol. 6, pp. 8302–8321, Jan. 2018.

[55] PureWavePolarizers Ltd. *10 MICRON WIRE GRID POLARIZER*. Accessed: Dec. 27, 2020. [Online]. Available: https://www.purewavepolarizers.com/wire-grid-polarizers/10-micron-wire-far-ir-thz-polarizer

SANG-HEE SHIN (Graduate Student Member, IEEE) was born in Seoul, South Korea, in 1992. He received the M.Eng. degree in aeronautical engineering from Imperial College London, London, U.K., in 2018, where he is currently pursuing the Ph.D. degree with the Department of Electrical and Electronic Engineering. His research interests include designing and manufacturing RF and quasi-optical systems for microwave and mm-wave applications using additive manufacturing techniques.

XIAOBANG SHANG (Senior Member, IEEE) received the B.Eng. degree (Hons.) in electronics and communication engineering from the University of Birmingham, Birmingham, U.K., in 2008, the B.Eng. degree in electronics and information engineering from the Huazhong University of Science and Technology (HUST), Wuhan, China, in 2008, and the Ph.D. degree in microwave engineering from the University of Birmingham, in 2011.

He is currently a Senior Research Scientist with the National Physical Laboratory, Teddington, U.K. He has authored or coauthored more than 70 scientific articles on microwave measurements and microwave circuits.

Dr. Shang was a recipient of several prestigious awards, including the ARFTG Microwave Measurement Student Fellowship Award in 2009, the IEEE Tatsuo Itoh Award in 2017, and the ARMMS Steve Evans-Pughe Prize in 2017. He has been serving as an Associate Editor for the IEEE Microwave and Wireless Components Letters, since 2020.

NICK M. RIDLER (Fellow, IEEE) received the B.Sc. degree in physics from King's College London, University of London, London, U.K., in 1981.

He is currently the Head of Science with the U.K. National Physical Laboratory, Department of Electromagnetic and Electrochemical Technologies, Teddington, U.K. He is also an NPL Fellow and a Visiting Professor with the University of Leeds, the University of Liverpool, and the University of Surrey, U.K., and a Nonexecutive Director of LA Techniques, Ltd. He has about 40 years of experience working in industrial, government, and academic research establishments. His main research interest includes precision high-frequency electromagnetic measurement (from 1 kHz to 1 THz). He is a Fellow of the Institution of Engineering and Technology (IET) and the Institute of Physics (IOP).

STEPAN LUCYSZYN (Fellow, IEEE) received the Ph.D. degree in electronic engineering from King's College London, University of London, London, U.K., in 1992, and the D.Sc. degree (higher doctorate) in millimeter-wave and terahertz electronics from Imperial College London, London, U.K., in 2010.

He is currently a Professor of Millimetre-Wave Systems at Imperial College London. He has coauthored well over 200 articles and 12 book chapters in applied physics and electronic engineering.

Prof. Lucyszyn was a Fellow of the Institution of Electrical Engineers, U.K., and the Institute of Physics, U.K., in 2005. In 2008, he became a Fellow of the Electromagnetics Academy, USA. He was appointed an IEEE Distinguished Microwave Lecturer, from 2010 to 2013. He co-founded the Imperial College London spin-out company Drayson Wireless Ltd., in 2014.

• • •